HHS Public Access

Author manuscript

Neuron. Author manuscript; available in PMC 2024 March 01.

Published in final edited form as:

Neuron. 2023 March 01; 111(5): 711–726.e11. doi:10.1016/j.neuron.2022.12.006.

Brainstem serotonin neurons selectively gate retinal information flow to thalamus

Jasmine D.S. Reggiani[1,2,3], **Qiufen Jiang**[2], **Melanie Barbini**[1], **Andrew Lutas**[1,5], **Liang Liang**[1,2,6], **Jesseba Fernando**[1], **Fei Deng**[4], **Jinxia Wan**[4], **Yulong Li**[4], **Chinfei Chen**[2,3,*], **Mark L. Andermann**[1,3,*,#]

[1.] Division of Endocrinology, Diabetes, and Metabolism, Beth Israel Deaconess Medical Center, Harvard Medical School, Boston, MA 02115, USA

[2.] F.M. Kirby Neurobiology Center, Boston Children's Hospital, Harvard Medical School, Boston, MA 02115, USA

[3.] Program in Neuroscience, Harvard Medical School, Boston, MA 02115, USA

[4.] State Key Laboratory of Membrane Biology, Peking University School of Life Sciences; PKUIDG/McGovern Institute for Brain Research, Beijing 100871, China

[5.] Present address: Diabetes, Endocrinology, and Obesity Branch, National Institute of Diabetes and Digestive and Kidney Diseases, National Institutes of Health, Bethesda, MD 20892, USA.

[6.] Present address: Department of Neuroscience, Yale University, New Haven, CT 06510, USA

SUMMARY

Retinal ganglion cell (RGC) types relay parallel streams of visual feature information. We hypothesized that neuromodulators might efficiently control which visual information streams reach the cortex, by selectively gating transmission from specific RGC axons in the thalamus. Using fiber photometry recordings, we found that optogenetic stimulation of serotonergic axons in primary visual thalamus of awake mice suppressed ongoing and visually evoked calcium activity and glutamate release from RGC boutons. Two-photon calcium imaging revealed that serotonin axon stimulation suppressed RGC boutons that responded strongly to global changes in luminance more than those responding only to local visual stimuli, while the converse was true for suppression induced by increases in arousal. Converging evidence suggests that differential expression of the 5-HT1B receptor on RGC presynaptic terminals, but not differential density

[*]**Corresponding authors:** Mark L. Andermann, manderma@bidmc.harvard.edu, Chinfei Chen, chinfei.chen@childrens.harvard.edu.
[#]Lead contact: Mark Andermann

Author contributions

J.D.S.R., C.C. and M.L.A. conceived of the project and wrote the manuscript. J.D.S.R. performed two-photon imaging experiments. Q.J. performed whole-cell recordings. J.D.S.R. and M.B. performed surgeries, photometry and immunohistochemistry experiments. F.D., J.W. and Y.L. developed the serotonin sensor. J.F. analyzed projection datasets from the Allen Brain Institute. A.L. helped build photometry and two-photon imaging set-ups. L.L. and J.D.S.R. wrote analysis pipelines. J.D.S.R. analyzed the data.

Declaration of interests

J.W. and Y.L. have filed patent applications, the value of which might be affected by this publication.

of nearby serotonin axons, may contribute to the selective serotonergic gating of specific visual information streams before they can activate thalamocortical neurons.

eTOC blurb

Reggiani et al. find that, in awake mouse primary thalamus, serotonin from brainstem inputs suppresses retinal axon bouton presynaptic calcium signals and glutamate release. Different retinal axon classes were more strongly suppressed by serotonin vs. by pupil-linked arousal, indicating diverse gating of visual information streams before they activate thalamocortical neurons.

Graphical Abstract

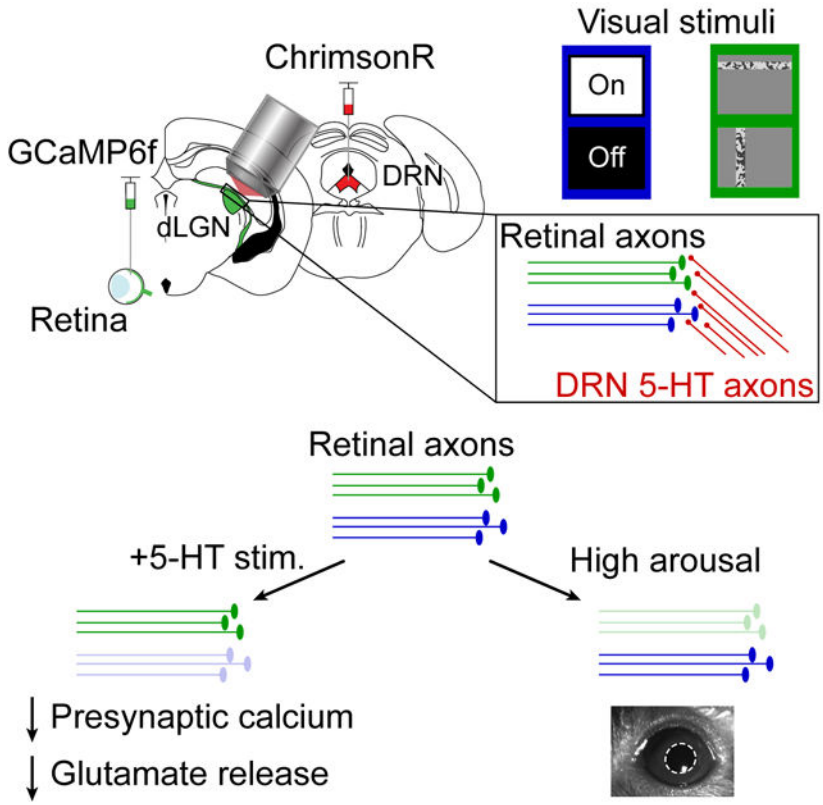

Keywords

Serotonin; 5-HT; 5-HT1B; htr1b; dLGN; thalamus; retina; retinal ganglion cell axons; two-photon calcium imaging; fiber photometry; glutamate release; luminance; neuromodulation; neuromodulator; dorsal raphe nucleus

INTRODUCTION

The relay of sensory information from the periphery to the cortex is integral to perception. The thalamus is a critical hub in this process, as information that effectively drives thalamocortical neurons is then amplified and processed by orders of magnitude more neurons in primary sensory cortex [1,2]. Perception is also strongly influenced by internal

states, which are encoded in a distributed manner by diverse neuromodulatory neurons. States such as locomotion and arousal (indexed by large pupil area) can modulate responses in primary sensory afferents [3,4], thalamic neurons [5–9] and cortical neurons [10–16]. The activity of neuromodulatory neurons such as those that release norepinephrine or acetylcholine is tightly coupled to changes in locomotion and arousal [17–21]. Serotonergic neurons in the dorsal raphe nucleus (DRN) of the brainstem are also associated with internal states, yet different serotonin neurons exhibit variable and context-dependent coupling to locomotion and arousal [22,23]. The nature and mechanisms by which any given population of neuromodulatory inputs shapes the content of sensory processing remain poorly understood. While regulation of the overall gain in sensory information flow in thalamus and cortex by distinct neuromodulators has been investigated both *in vivo* [24–27] and in brain slice experiments [28–30], less is understood about the *selective* modulation of specific information channels. We therefore investigated the actions of a single neuromodulator, serotonin, on functionally diverse retinal inputs to the thalamus *in vivo*.

Retinal axons in thalamus are uniquely suited for investigating neuromodulatory gating, for several reasons. First, retinal ganglion cells (RGCs) are among the best understood neuronal types in the mammalian brain at a molecular and functional level [31–34]. Second, unlike reciprocally connected downstream regions, retinal inputs comprise a simpler, unidirectional flow of multiple parallel information streams. These distinct streams show various degrees of convergence onto thalamocortical cells, resulting in combinatorial or more relay-like modes of transmission of information regarding global changes in luminance, direction of motion, and fine details in the visual scene [35–39].

Serotonin is known to modulate transmission of early visual information in the dorsolateral geniculate nucleus of the thalamus (dLGN) [40,41], suprachiasmatic nucleus [42,43] and superior colliculus [44], as well as early olfactory and auditory information [45,46]. In particular, pharmacological delivery of high doses of serotonin or associated agonists in brain slices decreases retinal axon stimulation-evoked glutamate release via presynaptically expressed 5-HT1B receptors [40–42]. Whether endogenous release of serotonin appreciably modulates the activity of mouse retinal axonal boutons *in vivo*, and whether this modulation is selective to specific retinal axons, remains unknown.

To address these questions, we developed methods for optogenetic stimulation of dorsal raphe serotonergic axons in dLGN ($DRN^{5HT\rightarrow dLGN}$) *in vivo* and *in vitro* during optical and electrophysiological recordings of retinal axonal activity and glutamate release. $DRN^{5HT\rightarrow dLGN}$ axon stimulation suppressed calcium activity and glutamate release in RGC axonal boutons. This suppression was greater in boutons strongly driven by global luminance changes than in those driven only by local stimuli, while the converse was true for suppression during high arousal (which likely involves other neuromodulators). Based on brain slice electrophysiology, immunohistochemistry, anatomical projections, and single cell sequencing data, we propose that differential *htr1b* receptor gene expression and presynaptic 5-HT1B receptor density across RGC types may contribute to the selective suppression of specific retinal axonal boutons.

RESULTS

Optogenetic stimulation of serotonin axons in visual thalamus suppresses retinal axons

We first combined optogenetics with fiber photometry in dLGN of awake, head-fixed mice to study the effects of endogenous release of serotonin on RGC axon terminals. To photostimulate serotonergic axons, we expressed a Cre-dependent, red-shifted channelrhodopsin ChrimsonR 93) in serotonergic neurons of the DRN (in Pet1-Cre mice) and implanted an optic fiber in dLGN. We then performed fiber photometry during optogenetic stimulation of $DRN^{5HT \rightarrow dLGN}$ axons through the same optic fiber (Fig. 1A, Fig. S1A; [47]). We first confirmed that photostimulation of $DRN^{5HT \rightarrow dLGN}$ axons evoked release of serotonin *in vivo,* by viral expression in the dLGN of a next-generation optical sensor for serotonin, $GRAB_{5\text{-}HT2h}$ (hereafter, $GRAB_{5\text{-}HT}$; [48]). Serotonin axon photostimulation drove an increase in $GRAB_{5\text{-}HT}$ fluorescence throughout the stimulation period, indicating increased serotonin release (Fig.1B-C; no effect in Pet1-$Cre^{-/-}$ animals, S1C). This photostimulation protocol did not alter global arousal [49,50], as it did not drive consistent changes in either pupil size or locomotion (Fig. 1D). Large increases in $GRAB_{5\text{-}HT}$ fluorescence upon systemic administration of the selective serotonin reuptake inhibitor fluoxetine confirmed that serotonin is spontaneously released in dLGN (Fig. S1B, D). We also observed slow spontaneous fluctuations in $GRAB_{5\text{-}HT}$ fluorescence across several tens of seconds, of a similar magnitude to those evoked by optogenetic stimulation (Fig. S1E). Thus, our stimulation protocol likely evoked serotonin release at physiological, non-saturating levels.

We then expressed GCaMP6f unilaterally in RGCs and paired $DRN^{5HT \rightarrow dLGN}$ axon photostimulation with fiber photometry recordings from RGC axons in contralateral dLGN (Fig. 1E, S1F). To evoke visual responses in RGC axons, we presented sinusoidal gratings. During a subset of presentations, we photostimulated $DRN^{5HT \rightarrow dLGN}$ axons for 6 s, beginning 3 s prior to visual stimulus onset. Photostimulation caused a reduction in calcium activity at baseline (uniform mean luminance), prior to visual stimulus onset, and a small additional reduction in activity during the visual stimulus (Fig. 1F, H-I, Fig. S1G-H). Such suppression was not affected by pupil size or eye motion (Fig. S1I-M), and was absent in control Pet1-$cre^{-/-}$ mice that received photostimulation but did not express ChrimsonR (Fig. 1G-I, S1H). The reduction in baseline axonal calcium signals could be due to suppression of spiking-independent presynaptic calcium (e.g. from subthreshold membrane depolarization or internal stores), or of spontaneous spiking-related axonal calcium [32]. We confirmed that $DRN^{5HT \rightarrow dLGN}$ photostimulation suppressed spiking-related calcium signals in RGC axons at baseline, as this suppression was blocked by intraocular injection of tetrodotoxin (TTX, [51]; Fig. 1J-K).

Given that the retinothalamic synapse exhibits strong presynaptic depression [52], it was unclear whether the serotonergic suppression of baseline spiking-related calcium signals would have a significant effect on baseline glutamate release. Thus, we recorded glutamate release from RGC axons in dLGN following intraocular injection of an optical sensor of glutamate (AAV-iGluSnFR.A184S, [53,54]; Fig. 1L, S1N). This approach biased the recordings towards glutamate release from retinal boutons vs. cortical boutons – the other major source

of glutamatergic input [55] – as these two groups of boutons are largely segregated spatially in dLGN (Fig. S1O). Accordingly, we observed short-latency increases in glutamate release during presentation of visual stimuli (Fig. 1M). As with calcium signals, $DRN^{5HT \rightarrow dLGN}$ photostimulation suppressed glutamate release from retinal axons at baseline, with a small additional suppression of release during visual stimuli (Fig. 1M-N, S1P). The suppression of glutamate release at baseline was spiking-related, as it was blocked by intraocular injection of TTX (Fig. 1O). Taken together, these findings show that activation of serotonergic axons in dLGN suppresses ongoing and visually evoked, spiking-related calcium signals in RGC axons, resulting in reduced glutamate release.

Suppression of baseline calcium signals in individual RGC boutons across the surface of dLGN

The above photometry recordings, which pooled signals across many RGC axons, demonstrate that endogenous serotonin release suppresses overall calcium levels in RGC axons. To investigate whether this suppression differs across individual RGC boutons, we paired the same viral strategy as in Figure 1E-F with two-photon calcium imaging of individual boutons via an imaging window that was chronically implanted above the dorsal surface of dLGN (Fig. 2A-B, [3,35]; adapted from [56]). We initially imaged at low magnification (1160 × 660 μm^2 field of view [FOV], 50 μm below the imaging window) to visualize RGC boutons across the entire dorsolateral extent of the dLGN (Fig. 2C, top). We also visualized ChrimsonR-tdTomato expression of $DRN^{5HT \rightarrow dLGN}$ axons (Fig. 2C, middle). We identified the region of the FOV that receives inputs from ipsilateral RGC axons (‘ipsilateral patch’) using anterograde CTB-Alexa647 injection into the ipsilateral eye following functional imaging sessions (Fig. 2C, bottom). This allowed us to align FOVs across mice (Fig. S2A-B) and to a digital atlas of axonal projections from all RGCs to dLGN (the Allen Brain Connectivity Atlas; Fig. S2C-D), confirming the location of our FOVs within the thalamus and within the dLGN (Fig. S2E).

To compare serotonergic suppression across individual boutons during spontaneous activity at baseline, we photostimulated $DRN^{5HT \rightarrow dLGN}$ axons through the imaging objective while the mouse viewed a mean luminance gray screen (photostimulation did not affect global arousal, Fig. S2F). Photostimulation drove robust and reliable suppression in some boutons but not others (see example boutons in Fig. 2D and S2G and population analyses of visually responsive RGC boutons in Fig. 2E). Moreover, in each of the six mice, we observed a greater amplitude of suppression at baseline in visually responsive boutons located in anterior vs. posterior dLGN, and in medial vs. lateral dLGN (Fig. 2F-G, S2H-I).

Retinal boutons that strongly respond to full-field luminance changes are more suppressed at baseline

We next tested whether the variable degree of suppression across nearby boutons and throughout the dLGN was related to differences in the boutons’ visual tuning properties. We presented two types of visual stimuli which together drive a majority of RGCs [34]: full-field increments or decrements in luminance, and elongated bars containing binarized spatiotemporal white noise at 8 horizontal and 8 vertical positions on the screen ([3,35]; Fig. 3A). We identified 6,299 visually driven RGC boutons in 6 mice (Fig. 3A, S3A).

We classified boutons into 4 categories (Fig. 3A-B, S3A): those that responded, among the set of stimuli we presented, only to full-field luminance changes ('FF' boutons), only to white-noise bar stimuli ('Bar' boutons), to both full-field and bar stimuli ('FF+bar' boutons), and those that were suppressed by some bar stimuli but not activated by others (suppressed-by-contrast, 'SBC'; [35,57,58]). We found that FF boutons were more strongly suppressed at baseline by $DRN^{5HT \rightarrow dLGN}$ stimulation than Bar boutons (Fig. 3C).

Different RGC types are known to exhibit different ranges of ongoing and evoked firing [32], making it challenging to compare changes in fluorescence across their boutons. To address the possibility that differences in the range of firing or fluorescence levels across bouton categories might explain the differential suppression, we normalized each bouton's activity between 0 and 1 (i.e. between the lowest and highest fluorescence levels of its dynamic range, defined using a large battery of stimuli in the absence of $DRN^{5HT \rightarrow dLGN}$ photostimulation; see Methods and Fig. 3B). The greater $DRN^{5HT \rightarrow dLGN}$-evoked suppression of FF vs. Bar boutons persisted when estimating the degree of suppression relative to each bouton's dynamic range (Fig. 3D).

We also considered whether differences in suppression of baseline activity across categories of RGC boutons could merely reflect differences in spontaneous activity levels. We found that boutons that were driven by bar stimuli containing white noise (Bar or FF+bar boutons) had substantially lower levels of baseline activity within their dynamic range as compared to FF and SBC boutons (Fig. 3E), which may prevent $DRN^{5HT \rightarrow dLGN}$-evoked suppression of baseline activity in bar-driven boutons due to a 'floor' effect. Indeed, we observed modest yet significant correlations between baseline activity and magnitude of $DRN^{5HT \rightarrow dLGN}$-evoked suppression across boutons, both across and within RGC categories (Fig. 3F). However, additional experiments (Fig. 4) ultimately showed that floor effects were not the cause of differences in amplitude of suppression across RGC categories.

Boutons in each category showed some degree of functional segregation along the anterior-posterior axis in dLGN (Fig. S3C). Specifically, boutons in the anterior dLGN did not exhibit retinotopic responses to white-noise bars, while most boutons in the posterior dLGN exhibited weaker or no responses to full-field changes in luminance (Fig. S3C, E-F). Boutons in anterior dLGN did exhibit retinotopic organization when presented with spatially restricted bars containing uniform increments or decrements in luminance (Fig. S3E). To better understand this spatial organization, we aligned our imaging FOVs to the Allen Brain Connectivity Atlas of projections from various genetically-defined RGC cell types to different regions of dLGN (Fig. S2A-E). This revealed that functionally distinct RGC types innervate different regions of dLGN in a manner similar to the partial segregation of FF and Bar boutons in our FOV (Fig. S3C-D). While we cannot prove that our bouton categories map onto these RGC types, these findings illustrate spatial segregation of functionally and genetically diverse retinal inputs in dLGN [59]. Relatedly, this segregation may arise in part from the slight tilt in our imaging plane such that anterior and posterior aspects of each FOV sampled from core and shell regions of dLGN, respectively. Notably, FF boutons were more strongly suppressed by $DRN^{5HT \rightarrow dLGN}$ photostimulation than Bar boutons even when restricting analyses to regions of posterior dLGN where Bar and FF boutons were intermingled (Fig. 3G).

Activity-matched analyses confirm differential suppression of retinal boutons

To address the possibility that potential floor effects contribute to the differential suppression observed across RGC bouton categories, we considered how $DRN^{5HT\rightarrow dLGN}$ photostimulation might affect FF vs. Bar boutons at time points when, on control trials, each bouton's activity is far from the floor or ceiling of its dynamic range. This was achieved by carrying out additional experiments pairing photostimulation with presentation of two visual stimuli designed to drive FF and Bar boutons throughout their dynamic range: a 6-s sequence of full-field luminance changes (to drive FF boutons) and a 6-s sequence of short bars containing binarized spatiotemporal white noise (to drive Bar boutons; Fig. 4C, S4A, Movie S2, 7,914 boutons, 22 FOV, 9 mice), centered on the region of visual space that best drove retinal boutons in each FOV. This resulted in five types of trials (two stimuli, each presented with or without $DRN^{5HT\rightarrow dLGN}$ stimulation, as well as $DRN^{5HT\rightarrow dLGN}$ stimulation at baseline), delivered in pseudorandom order. To further characterize functional properties of these boutons, we also mapped their retinotopic preferences (Fig. S4B-C) and tuning for spatial frequency, direction and axis of motion (Fig. 4C, S4A; [3,35]). These experiments were carried out using smaller fields of view in the posterior dLGN (190 × 330 μm^2, 50–90 μm below the imaging window; Fig. 4A, B), to record from individual RGC terminals with greater sensitivity and spatial resolution, and to characterize serotonergic suppression from a larger population of Bar boutons concentrated in this region of dLGN (Fig. S3C). Despite these modifications to the imaging protocol, we reproduced the findings in Figs. 2–3 regarding differences in baseline activity and in the suppression of baseline activity by $DRN^{5HT\rightarrow dLGN}$ stimulation across RGC bouton categories (Fig. S4D).

We next examined the effects of $DRN^{5HT\rightarrow dLGN}$ photostimulation across boutons at times when, on control trials, each bouton's activity was at a particular level within its dynamic range. Fig. 4D illustrates our findings for example Bar and FF boutons. To assess the amplitude of the suppression at various levels within the dynamic range, we defined 1-s bins during and surrounding the two visual stimuli (Fig. 4D, orange bars) and computed the difference between activity levels on optogenetic stimulation trials (R_{opto}) and control trials (R_{ctrl}). We plotted this difference as a function of a bouton's dynamic range level at each moment on control trials. The example FF bouton in Fig. 4D was more suppressed than the example Bar bouton at each dynamic range level (Fig. 4E inset). Across all boutons, FF boutons were on average more strongly suppressed than other boutons at all levels within the dynamic range (Fig. 4E). We next focused on bins in which, on control trials, a bouton had a mean activity level between 0.5 and 0.7 of its full dynamic range (i.e. far from floor levels). This approach confirmed that suppression was significantly more common and pronounced for FF boutons than for other boutons (Fig. 4F). In particular, $DRN^{5HT\rightarrow dLGN}$ suppression was consistently greater for FF vs. Bar boutons across individual mice and across all imaged FOVs with sufficient numbers of both FF and Bar boutons (Fig. 4G, S4E-F). Together, these findings confirm that the differential suppression of FF vs. Bar boutons by $DRN^{5HT\rightarrow dLGN}$ stimulation is not due to floor effects.

We also considered the intermediate category of boutons driven by both full-field luminance changes and local bars containing white noise (FF+bar boutons). Within this category, $DRN^{5HT\rightarrow dLGN}$ suppression was greater for boutons preferring lower spatial frequency

gratings (down to 0.02 cycles/degree, a stimulus involving coherent changes in luminance across most of the screen), and thus were more sensitive to near-full-field luminance changes (Fig. 4H, S4G). Thus, across RGC categories, $DRN^{5HT \rightarrow dLGN}$ stimulation appears to drive greater suppression of boutons with higher sensitivity to coherent changes in luminance. In contrast, suppression was not related to a bouton's direction or axis selectivity (Fig. S4H).

Modulation of distinct retinal boutons by $DRN^{5HT \rightarrow dLGN}$ stimulation or arousal

We next considered potential relationships between serotonin release and arousal in dLGN, as arousal also tends to suppress visual responses to varying degrees across functionally distinct groups of RGC boutons in dLGN [3]. DRN serotonin neurons, on average, are generally more active during waking vs. sleep states [50,60]. However, in contrast to noradrenaline and acetylcholine levels that tightly correlate with rapid changes in arousal or locomotion [19], the relationship of serotonin levels with arousal/locomotion is weaker and more nuanced [22]. Indeed, individual DRN serotonin neurons can show either increased or decreased activity during locomotion [23], and the functional properties of the subset that projects to dLGN remains unknown. We combined fiber photometry of the serotonin sensor $GRAB_{5\text{-}HT}$ in dLGN with recordings of pupil size and locomotion (Fig. 5A-B), as well as with delivery of tail shocks and drops of milkshake (Ensure) in a subset of recordings [61–63]. These salient stimuli led to changes in arousal (pupil size and/or running speed), but did not increase serotonin release in dLGN, and instead drove very modest decreases in serotonin (Fig. S5B-C). We also observed a modest negative correlation between the large spontaneous fluctuations in $GRAB_{5\text{-}HT}$ fluorescence (Fig. 5B, S1E) and pupil area (Fig. 5B-C, S5D). However, changes in pupil area only explained about 7% of the variance in $GRAB_{5\text{-}HT}$ fluorescence (Fig. 5C), indicating that many of the larger spontaneous fluctuations in local serotonin levels in dLGN could not be explained by arousal or other recorded behavioral variables (Fig. 5B,D).

We wondered how the level of arousal might affect the suppression of RGC bouton activity we observed during $DRN^{5HT \rightarrow dLGN}$ stimulation. We defined arousal level using the pupil area prior to trial onset, normalized to the maximum pupil area in each session [3]. Arousal level did not affect the amount of serotonin released by $DRN^{5HT \rightarrow dLGN}$ stimulation (Fig. S5E-F). Further, FF boutons were more suppressed by $DRN^{5HT \rightarrow dLGN}$ stimulation than Bar boutons (as in Fig. 4E-H), even when restricting analyses to trials with low or high levels of arousal (Fig. S5G). Thus, differential suppression of FF vs. Bar boutons by $DRN^{5HT \rightarrow dLGN}$ stimulation is not dependent on the level of arousal.

Next, using the same dataset as in Figure 4, we asked whether the same or different boutons were suppressed by serotonin axon stimulation and by arousal. Fig. 5E illustrates the visual responses on control trials (no optogenetic stimulation) of the same two example boutons as in Fig. 4D, but plotted separately for control trials during high or low arousal levels (i.e. trials in which the pre-stimulus pupil size was above or below 50% of maximum, respectively). While the Bar bouton is suppressed by arousal but not by $DRN^{5HT \rightarrow dLGN}$ stimulation (Fig. 4D, 5E), the converse is true for the FF bouton. Across the population, Bar boutons were more strongly suppressed by arousal than other boutons (Fig. 5F). These differences in arousal modulation were not explained by differences in modulation

of baseline activity across RGC categories (Fig. S5H). The scatter plot in Fig. 5G directly compares each bouton's degree of modulation by arousal vs. by $DRN^{5HT \rightarrow dLGN}$ stimulation. These two forms of modulation were not positively correlated across boutons, and instead were weakly but significantly anti-correlated. Across mice, FF boutons were more suppressed by $DRN^{5HT \rightarrow dLGN}$ stimulation than Bar boutons (Fig. 4G), but were *less* suppressed by arousal than Bar boutons (Fig. 5H, S5I). These findings demonstrate that, despite the relatively weak suppression of Bar boutons by $DRN^{5HT \rightarrow dLGN}$ stimulation (Fig. 4F), these boutons could be strongly suppressed in other contexts, such as during states of high arousal (Fig. 5F-H). We further confirmed that, during periods of high arousal, boutons preferring low vs. high spatial frequencies and decreases vs. increases in luminance (i.e., OFF versus ON) were more strongly suppressed (as previously shown[3], Fig. S5J-K). Notably, we found no difference in the amplitude of suppression between OFF- vs. ON-preferring boutons during $DRN^{5HT \rightarrow dLGN}$ stimulation (Fig. S5L), indicating additional differences in the visual information content suppressed during arousal vs. by $DRN^{5HT \rightarrow dLGN}$ stimulation. Thus, serotonin axon activity and arousal fluctuations during the awake state appear to act as distinct gates of different visual information streams from the retina to the thalamus and cortex.

Local DRN axon density does not explain the stronger suppression of FF boutons

At least three possible mechanisms could underlie the stronger suppression of FF vs. Bar boutons by $DRN^{5HT \rightarrow dLGN}$ stimulation: (i) differences in DRN axon density surrounding each bouton, (ii) differences in the presynaptic expression of the inhibitory serotonin receptor, 5-HT1B, and (iii) differences in downstream effectors within each bouton. We considered the first two possibilities in detail, focusing first on DRN axon density. Using binarized images of tdTomato-expressing DRN axons in each imaging FOV (Fig. 6A), we measured the local density of axons in a disk of 10 μm radius surrounding each bouton's center of mass. Using data from FOVs that spanned the dorsolateral surface of dLGN (Figs. 2–3), we found that DRN axon density near different boutons could vary substantially, but was on average uniform along both the A-P and M-L axes of dLGN in each mouse (Fig. S6A-B). Higher local DRN axon density was associated with a greater amplitude of baseline suppression by $DRN^{5HT \rightarrow dLGN}$ stimulation across all boutons (Fig. 6B). This suggests that the degree of bouton suppression likely scales with the overall level of serotonin released from nearby DRN axons. Critically, however, FF boutons were consistently more suppressed than Bar boutons, even when matching for similar levels of local DRN axon density (Fig. 6C-D). We also found that DRN axon density was variable across boutons but similar, on average, across bouton categories (Fig. 6E-F; data from higher-magnification FOVs in Figs. 4–5). Using data from higher-magnification FOVs, we also confirmed that FF boutons were more strongly suppressed than Bar boutons when considering activity levels within .5-.7 of their dynamic range on control trials, even when matching for similar levels of local DRN axon density (Fig. 6G-H, S6C-D). Taken together, these data indicate that DRN axon density explains some variability in the amplitude of serotonergic suppression but does not explain differences across bouton categories.

Differential 5-HT1B receptor expression may contribute to selective suppression

Previous work showed that RGCs express *htr1b* mRNA [64] and that agonists for this receptor can reduce glutamate release from RGC axons onto dLGN neurons in brain slices [40,41]. Using immunohistochemistry for 5-HT1B, we observed high levels of expression of this receptor throughout the LGN, but not in most neighboring thalamic nuclei other than ventral LGN (Fig. 7A). To investigate which sources of axonal input to dLGN expressed 5-HT1B receptors, we labeled all RGC axons with YFP (in Chx10-Cre;FLEX-ChR2-YFP mice; [38]) and stained for Vglut2, which selectively labels RGC synaptic terminals [65]. We found that 5-HT1B puncta were co-localized with RGC boutons (Fig. 7B). In addition, we observed minimal colocalization of 5-HT1B with primary visual cortex (V1) axons, the other main glutamatergic input to dLGN, or with $DRN^{5HT\rightarrow dLGN}$ axons, on which it would act as an autoreceptor (Fig. S7A). Accordingly, monocular enucleation (and subsequent RGC axon degeneration in dLGN) eliminated 5-HT1B expression in the contralateral dLGN (Fig. S7B).

We next tested whether the 5-HT1B receptor mediates suppression of glutamate release by $DRN^{5HT\rightarrow dLGN}$ stimulation using whole-cell patch clamp recordings from thalamocortical neurons in dLGN brain slices from Pet1-Cre mice expressing ChrimsonR-tdTomato in DRN (Fig. S7C). We paired optic tract electrical stimulation (to evoke retinothalamic excitatory postsynaptic currents [EPSCs]) with optogenetic activation of $DRN^{5HT\rightarrow dLGN}$ axons (Fig. 7C). $DRN^{5HT\rightarrow dLGN}$ photostimulation transiently suppressed peak evoked AMPAR EPSC amplitudes (Fig. 7D-F), consistent with our previous findings using bath application of serotonin [40,41]. Critically, subsequent bath application of a 5-HT1B antagonist (NAS-181, 10 μM, [66]) blocked the suppressive effect of $DRN^{5HT\rightarrow dLGN}$ axon photostimulation (Fig. 7G, S7D-E). Because $GABA_B$ receptors also modulate RGC axons presynaptically [40], we considered whether the effects of $DRN^{5HT\rightarrow dLGN}$ axon photostimulation could be due in part to GABAergic suppression of RGC axons, either by indirect, serotonin-evoked GABA release from dLGN interneurons [28,67] or by co-release of GABA from $DRN^{5HT\rightarrow dLGN}$ axons [68]. However, bath application of a $GABA_B$ antagonist (CGP-55845, 2 μM) did not alter the suppression caused by $DRN^{5HT\rightarrow dLGN}$ stimulation (Fig. S7F-H). Taken together, our results suggest that $DRN^{5HT\rightarrow dLGN}$ stimulation-evoked suppression of RGC axons is mediated by expression of the 5-HT1B receptor on RGC axon terminals.

To assess whether *relative* levels of 5-HT1B expression differed across molecularly defined RGC types, we first evaluated *htr1b* mRNA expression in a publicly available single-cell RNA-seq dataset of adult RGCs [33]. Expression of *htr1b* in RGCs was higher than other serotonin receptors (Fig. S7I). Further, molecularly-defined RGC types showed reliably different levels of *htr1b* expression (Fig. 7H). To confirm that these differences in somatic *htr1b* expression corresponded to differences in 5HT1B expression at RGC terminals, we labeled with YFP the axons of two groups of RGC types that have very different levels of *htr1b* expression (Fig. 7H): alpha RGCs (labeled by Kcng4-Cre, [69]) and F-mini RGCs (labeled by Foxp2-cre,[70]). Notably, in comparison to F-mini RGCCs, alpha RGCs have relatively higher responses to large equiluminant stimuli, higher levels of baseline activity (Fig. S7J-K, [32,70,71]), and their axons project to more anterior parts of our dLGN FOV (Fig. S3D). This suggests a potential partial overlap of our imaged FF boutons with the alpha RGCs and of bar-driven boutons with F-mini RGCs. We found that, compared to

5-HT1B expression in all RGC boutons in dLGN, expression was substantially lower in F-mini RGC boutons than in alpha RGC boutons (Fig. 7I, S7L). Thus, differences in mRNA expression were predictive of levels of presynaptic protein. While indirect, these electrophysiological, molecular, anatomical and immunohistochemical results suggest that differential presynaptic expression of the 5-HT1B receptor may contribute to the differential serotonergic suppression of FF vs. Bar RGC boutons observed *in vivo*.

DISCUSSION

There is a growing number of studies investigating how internal states such as arousal affect sensory processing. While internal states correlate with the activity of many neuromodulators, a major unresolved question in neuroscience is how any one neuromodulator contributes to selective sensory processing. We found that serotonergic axons suppress calcium signals and glutamate release in retinal boutons. Moreover, suppression by endogenous serotonin release in dLGN was more pronounced in subsets of retinal axonal boutons that responded more strongly to global changes in luminance than to local visual stimuli, while the converse was true for suppression that occurred during increases in arousal.

Serotonergic modulation of synaptic transmission and convergent retinal inputs

We investigated two potential mechanisms underlying the stronger $DRN^{5HT\rightarrow dLGN}$ stimulation-evoked suppression of FF vs. Bar boutons. First, we found that local DRN axon density correlates with the degree of suppression but does not explain differences across bouton categories. In contrast, converging evidence suggests a possible role for differential expression of the 5-HT1B receptor, a $G_{i/o}$-protein coupled receptor, on different RGC presynaptic terminals (in addition to other potential mechanisms such as effectors downstream of 5-HT1B). Presynaptic G-protein coupled receptors are increasingly recognized as key regulators of neuronal communication throughout the brain [72]. However, few mammalian studies have addressed this mechanism in well-characterized sets of projection neurons or *in vivo*. Previous studies using brain slices have shown that bath-applied serotonin suppresses glutamate release from RGC axons by reducing spike-evoked calcium entry into the presynaptic terminal [40–42,44]. Our results demonstrate that $DRN^{5HT\rightarrow dLGN}$ stimulation *in vivo* reduces the amount of calcium evoked in RGC axonal boutons. Indeed, 5-HT1B is thought to inhibit adenylyl cyclase and attenuate calcium influx through voltage-gated calcium channels [66,73,74]. Previous studies have demonstrated a monotonic, albeit nonlinear relationship between presynaptic calcium and glutamate release [75–77]. Accordingly, we observed $DRN^{5HT\rightarrow dLGN}$ stimulation-evoked suppression of both baseline and evoked bulk glutamate release from RGC axons.

In the dLGN, visual information from RGC axons is relayed to cortex-projecting thalamic neurons. Several recent studies have shown that mouse RGC axons can converge onto neurons in the thalamus [35,36,38,39], where they shape the tuning properties of their postsynaptic partners [37]. In cases where a thalamocortical cell receives input from several types of RGCs with distinct visual tuning, the relative weight of these inputs can powerfully influence the response properties of the target cell [37]. Our findings show that serotonin

preferentially suppresses RGC axonal boutons that exhibit high baseline activity and that respond to full-field stimuli (this category of boutons is likely composed of many functional subtypes of RGCs, each demonstrating distinct tuning for other visual features). At least some convergence of FF and Bar RGC boutons onto a dLGN dendrite is likely [35]. Further, we have observed immunolabeling of 5-HT1B in some but not all RGC terminals within clusters of converging RGC boutons (not shown). In this way, selective suppression by serotonin might shift the tuning of the postsynaptic cell towards smaller, more local stimuli, similar to what has been observed in zebrafish [78]. Indeed, DRN electrical stimulation selectively reduces evoked activity in thalamocortical neurons with large receptive fields [79], consistent with our observations of greater suppression of FF boutons. Interestingly, serotonin depolarizes most thalamocortical neurons in brain slices via actions on 5-HT2 receptors [29,80,81], suggesting that information that does make it to the thalamocortical neurons may then be amplified.

The ethological context of serotonergic modulation at the retinothalamic synapse

We observed slow fluctuations in serotonin release in dLGN, a small proportion of which could be explained by weak anti-correlation with arousal levels. The behavioral contexts that drive these fluctuations in serotonin remain largely unclear, as do the roles of serotonergic suppression of retinothalamic transmission in shaping downstream visual processing and behavior. Future studies tracking serotonin release in dLGN and its effects on retinal transmission during natural behaviors [82,83] will help address these questions. For comparison, serotonin release from dorsal raphe axons in the optic tectum of zebrafish is elevated during periods of hunger and drives a shift in the tectal cell population responses towards representation of small objects, which might represent prey [78].

Multiple distinct filters of visual information content at the level of retinal axons

Internal states, particularly arousal and locomotion, can modulate visual processing in both the cortex and the thalamus [5–12,15,16]. Modulation of early sensory information flow by arousal has been demonstrated in retinal axons [3,4], yet the mechanisms underlying these effects are not yet well understood. Subsets of retinal axons can be modulated by metabotropic actions of several modulators, including serotonin, GABA, glutamate, adenosine, acetylcholine and norepinephrine [40,84,85]. Each of these signals might be released to varying degrees during different internal states. For example, metabotropic effects of GABA and glutamate on RGC axons could arise from direct, long-range excitatory inputs from cortex [86,87] due to disynaptic inhibition and neurotransmitter spillover from nearby synapses. In this study, we find that serotonin, similar to arousal [3], selectively gates visual information by suppressing calcium activity in a subset of retinal axons. However, while serotonin preferentially suppresses RGC axons strongly driven by full-field changes in luminance, arousal preferentially suppresses boutons driven more strongly by local stimuli. This opens up the exciting possibility that serotonergic axons and other modulatory inputs could enact multiple complementary, state-dependent selective filters of specific visual information channels at a key bottleneck in the pathway, before these channels reach thalamocortical neurons and are subsequently relayed and amplified in downstream brain areas guiding behavior and learning.

STAR Methods

RESOURCE AVAILABILITY

Lead contact—Further information and requests for resources and reagents should be directed to and will be fulfilled by the lead contact, Mark L. Andermann (manderma@bidmc.harvard.edu).

Materials availability—This study did not generate new unique reagents.

Code and data availability—All photometry and two-photon calcium imaging data and original code reported in this paper have been deposited at: https://research.bidmc.harvard.edu/datashare/DataShareInfo.ASP?Submit=Display&ID=6 Any additional information required to reanalyze the data is available upon request from the lead contact, Mark L. Andermann (manderma@bidmc.harvard.edu).

EXPERIMENTAL MODEL AND SUBJECT DETAILS

Animals—All animal care and experimental procedures were approved by the Beth Israel Deaconess Medical Center Institutional Animal Care and Use Committee and by the Boston Children's Hospital Institutional Animal Care and Use Committee. Animals were housed on a 12h light-dark cycle (all experiments performed during the light phase), with *ad libitum* access to water and standard chow. All *in vitro* and *in vivo* experiments were performed on both male and female mice. Fiber photometry, imaging and slice electrophysiology experiments were performed on hemizygous Pet1-Cre mice (wild-type littermates were used for control experiments). Immunohistochemistry experiments used Chx10-Cre;FLEX-ChR2-YFP [88,89], Foxp2-Cre [70], Kcng4-Cre [90], and Pet1-Cre;FLEX-ChR2-YFP [91].

METHOD DETAILS

Surgical procedures—All surgical procedures for *in vivo* and slice experiments were performed in 8–12 week-old (unless otherwise specified) anesthetized (isoflurane in O_2; 4% for induction, 1% for maintenance) mice. After surgery, animals were given Meloxicam (.5 mg/kg, s.c.) and monitored during recovery.

Virus injections: Intravitreal injections of adeno-associated virus (AAV) were used for infection of retinal ganglion cells in the right eye [3,35]. For monitoring calcium activity, 1.2 μl of AAV2/2.CAG.GCaMP6f.WPRE.SV40 (Boston Children's Hospital viral core, 1.37E+12 gc/ml; [92]) was injected gradually over 2 minutes. For monitoring glutamate release, 1.2 μl of AAV2/1.hSynapsin.SF-iGluSnFR.A184S (Addgene, 100uL 2.2 × 10^13 gc/ml; [53]) was injected. For visualizing ipsilateral retinal inputs to the dLGN in mice used for two-photon imaging experiments, we injected 500 nl of CTB-A647 (Thermofisher) in the left eye after all imaging sessions had been performed. For infection of dorsal raphe serotonergic neurons, we injected AAV2/1.hSyn.FLEX.ChrimsonR.tdTomato (Addgene, 4.1E12 gc/ml; [93]) in the dorsal raphe nucleus (75 nl in each location at: AP −4.25, −4.55, −4.85, ML 0, DV −2.9 mm from Bregma). For recordings using the serotonin sensor, we injected AAV2/9.hSyn.$GRAB_{5\text{-}HT2h}$ (WZ biosciences, 4.34 × 10^13 gc/ml; [48]) in the dLGN (150 nl at: AP −2.55, ML −2.3, DV −2.8 mm from Bregma).

For histology experiments involving labeling of F RGCs and alpha RGCs (Fig 7I, S7L) 1 μl of AAV2/2.FLEX.ReaChR.mCitrine (Boston Children's Hospital viral core; [94]) was injected into each eye of Foxp2-Cre (~75% of Foxp2-cre labeled cells are F-mini RGCs; [70]) and Kcng4-Cre (>90% of Kcng4-Cre labeled cells are alpha RGCs; [90]) mice in the first week after eye opening (P14–21).

For histology experiments labeling V1 axons in dLGN, we injected AAV2/1.hSyn.GCaMP6f.WPRE.SV40 (Addgene, 150 nl, AP −3, ML −4, DV −1.25 mm from Bregma).

Drug administration: For silencing of spiking in RGC cell bodies (Fig 1J, K, O), we injected 1 μl of TTX (1 mM, [51]) intravitreally in the right eye while the mouse was anesthetized (1% isoflurane). After injection, the mouse was allowed to recover and 30 minutes later was head-fixed on the wheel for photometry recordings.

For testing of spontaneous serotonin release in dLGN (Fig S1D), we injected fluoxetine (16 mg/kg) intraperitoneally while the mouse was awake and head-fixed for fiber photometry recordings. Ten minutes before injecting fluoxetine, in the same recording, we injected an equal volume (approximately 100 μl) of sterile isotonic saline i.p. to control for any potential effects of the needle injection on changes in $GRAB_{5\text{-}HT}$ fluorescence.

Monocular enucleation: Monocular enucleation was performed as in [95]. The mice (Chx10-Cre;FLEX-ChR2-YFP) were anesthetized (2% isoflurane). After trimming the eyelid margins, the optic nerve was cut with surgical scissors, the eye removed, and the eyelids were glued with cyanoacrylate. Mice were then allowed to recover and were sacrificed 10 days later.

Fiber implants: Two to three weeks after eye and dorsal raphe virus injections, optic fibers with a metal ferrule (400-μm-diameter core; multimode; numerical aperture [NA] 0.48; 3.0 mm length; Doric Fibers) were implanted over dLGN (at AP −2.55, ML −2.3, DV −2.8 mm from Bregma). Mice were anesthetized and placed on a heating pad (CWE) in a stereotaxic apparatus (KOPF). Ophthalmic ointment (Vetropolycin) was applied to the eyes. The fiber was implanted stereotaxically through a small burr hole over the dLGN, by slowly lowering it perpendicular to the surface of the skull. The fibers and a custom-made two-pronged titanium headpost were then affixed to the skull with C&B Metabond (Parkell), as in [47]. Care was taken to fix the headpost parallel to the skull to ensure the head of the mouse was level when head-fixed and standing on a wheel during recordings. Mice were given at least two weeks to recover before photometry recordings.

Cannula implants: Two to three weeks after eye and dorsal raphe virus injections, a cranial window and headpost were implanted as detailed in [35] and [3]. Briefly, mice were given 0.03 ml of dexamethasone sodium phosphate (4 mg/ml, i.m.) roughly 3 h prior to surgery to reduce brain edema. Mice were anesthetized and placed on a heating pad (CWE) in a stereotaxic apparatus (KOPF). Ophthalmic ointment (Vetropolycin) was applied to the eyes. A two-pronged headpost was affixed to the skull, centered roughly 2.7 mm lateral and 2 mm posterior to Bregma over the left hemisphere, tangential to the curved skull

surface. The angle of the headpost with respect to the levelled skull was measured at this stage to ascertain the angle of the imaging window with respect to the dLGN. The head was then tilted to secure the headpost in custom clamps (Thorlabs) that aligned the headpost precisely parallel to the platform of the stereotaxic apparatus. A 3-mm diameter craniotomy was performed at the center of the headpost. The underlying cortical and hippocampal tissue was carefully aspirated until the surface of the thalamus was reached. The thalamic surface and optic tract were kept intact. A 3-mm diameter coverslip (glued to the bottom of a 3 mm x 3.4 mm [diameter x height] stainless steel cylindrical cannula [MicroGroup] prior to surgery using UV-cured Norland Optical Adhesive 71) was lowered into the craniotomy, approximately 2.75 mm below the skull, where it pressed slightly on the surface of the thalamus. The cannula was affixed to the skull with Vetbond (3M) followed by C&B Metabond (Parkell), to form a permanent seal. A well (made of Buna-N O-rings [McMaster-Carr] and dental cement) was built around the perimeter of the headpost which during imaging served the purposes of retaining water for the water-immersion objective and supporting a light shield that covered the objective to block the light from the LCD screen during two-photon imaging. Mice were allowed at least two weeks to recover before two-photon imaging.

Recordings

Fiber photometry recordings and associated optogenetic and visual simulation: Fiber photometry recordings were performed in awake behaving mice, head-fixed and placed on a running wheel [47]. The same optic fiber was used for recording of fluorescence signals (50–150 uW, 465 nm excitation, sampled at 1000 Hz) and optogenetic stimulation (6 s, 20 Hz, 10 ms pulses, 5 mW, 620 nm excitation, as in [47]). The eye contralateral to the placement of the fiber was facing a monitor (Dell 17″, 1280×1024 pixels, 60 Hz refresh rate) which displayed a mean luminance grey screen except for periods of visual stimulus presentation (sinusoidal grating, 2 s, .08 cycles per degree [cpd], 0° [vertical gratings moving from nasal to temporal], 2 Hz, 80% contrast, except for recordings in two $Pet1^{-/-}$ control mice in Fig. 1H-I in which full screen binarized white noise was used). The monitor was placed 25 cm from the mouse's face at approximately 45° from the mouse's body axis, roughly parallel to the angle of the mouse's face, spanning 15°−90° in azimuth and 45° degrees of elevation (Figure S3B). We used four types of trials: trials with visual stimulus presentation with or without optogenetic stimulation, and trials without visual stimuli ('blank' trials, in which the mouse is looking at a mean luminance gray screen) with or without optogenetic stimulation. In fiber photometry recordings of presynaptic calcium (GCaMP in RGC axons), we presented all four types of trials. In fiber photometry recording of serotonin release ($GRAB_{5\text{-}HT}$), we presented only 'blank' trials with or without 6 s of optogenetic stimulation. For fiber photometry recordings of glutamate release (iGluSnFR in RGC axons), we only presented trials with the same visual stimuli in the presence or absence of optogenetic stimulation. All trials were presented in pseudorandom order. Inter trial intervals lasted 6 s. In each recording session we presented between 100 and 300 trials in total (approximately 50–150 per trial type). Locomotion and pupil area were tracked during recording sessions (sampled at 15 Hz, as in [47]). Visual and optogenetic stimuli were presented using NIMH MonkeyLogic or NIMH ML1.

Dual color fiber photometry recordings: Fiber photometry experiments with dual-color excitation were carried out (as described in [96]) in mice expressing $GRAB_{5\text{-}HT}$ in the dLGN, using a 465-nm LED and a 405-nm LED to excite the fluorophore near its isosbestic point (425 nm). The two light sources, controlled by Plexon LED drivers, were coupled to a Doric mini cube that converged the light onto a single patch cord. Alternating square pulses (6 ms) of each LED were delivered at 50 Hz through the patch cord to the fiber optic cannula. Emitted fluorescence was collected through the patch cord and recorded on a photoreceiver. Locomotion and pupil area were tracked during these recording sessions (sampled at 15 Hz). A subset of recording sessions included the delivery of tail shocks (.4 mA, 2 × 50 ms, 100 ms inter-shock interval, delivered via two electrode pads wrapped around the base of the tail) and drops of milkshake (Ensure, ~5 ul) to chronically food restricted mice (maintained at 80–85% body weight; [47]; Fig 5D, S5B-C). These appetitive and aversive stimuli were delivered 30 or 60 s apart. In a subset of recording sessions, we switched between 5-minute blocks in which mice received repeated shocks, Ensure deliveries or no stimuli.

Two-photon imaging: Two-photon calcium imaging was performed as in [35] and [3] using a resonant-scanning two-photon microscope (Neurolabware) and an Insight X3 laser (80 MHz; Spectra-Physics; 920 nm for GCaMP6f, 1060 nm for ChrimsonR-tdTomato visualization, 1200 nm for A647). All images were acquired using a 10x, 0.6 NA, 8 mm WD water immersion objective (Olympus) at 6.7x (190 × 330 μm^2; Figs. 4–6) or 1.7x (1160 × 660 μm^2; Figs. 2–3, 6) digital zoom. For experiments in which the FOV encompassed the entire surface of dLGN (Figs. 2–3, 6), we imaged at 50 μm below the surface of the optic tract. For experiments using higher magnification (Figs. 4–6), we imaged at 50–90 μm below the surface of the optic tract. Images were collected at 15.5 frames/s, using Scanbox (Neurolabware). Each imaging run lasted approximately 30 mins, and 4–5 runs were performed during each imaging session. Occasionally, the imaging depth was adjusted slightly in between runs to account for small, slow drifts in the z-plane.

For optogenetic stimulation of ChrimsonR, light was delivered through the imaging objective, using a 617 nm LED (2.6 mW at base of cannula; M617L3; ThorLabs) bandpass filtered (630–669 nm; Thorlabs, FBH650–40; designed to avoid stray light at wavelengths detected by the mouse retina) and controlled by an LED driver (T-Cube; ThorLabs), synchronized with fluorescence image acquisition (15.5 Hz; 8 ms; [97]).

For tracking the arousal state of the animal, the pupil ipsilateral to the LCD screen was trans-illuminated by the spread of two-photon excitation infrared light (920 nm) emanating from within the brain. Images of a pre-selected region of interest around the eye were recorded using a CCD camera (Dalsa) at 15.5 Hz, and synchronized with fluorescence image acquisition (Scanbox, Neurolabware).

Visual stimulation and optogenetic stimulation during two-photon imaging: Visual stimuli were presented to the mouse on a LCD monitor (Dell, 17″, 1280×1024 pixels, 60 Hz refresh rate) placed 25 cm from the mouse's right eye, and parallel to the angle of the mouse's face. Visual inspection at the beginning of each imaging session confirmed that the whole monitor was visible to the mouse and no part of it was blocked by the objective or the

light shielding around it. As is illustrated in the diagram in Fig. S3B, the monitor spanned approximately 75° in azimuth (centered on the mouse's pupil) from 15° to 90° in azimuth (along the mouse's body axis), and spanned 46° in elevation from 0° to 46° above the level of the pupil (in a small subset of recordings the monitor was lowered by 7° to center it on the area of visual space encoded by a FOV; the resulting retinotopic preferences were adjusted by 7° to match the other recordings). The mean luminance of the monitor was 8.6 lux. Imaging sessions usually consisted of several 'runs' (recording periods of approximately 30 minutes each). An imaging session started with two runs in which optogenetic stimulation was delivered (either paired with the presentation of visual stimuli or during presentation of a mean luminance gray screen, see below), followed by one retinotopy run in which we presented noise bars and full-field luminance changes to characterize the retinotopic preference of boutons and classify them into the four functional categories (see below). For FOVs collected at high magnification (Figure 4–5), these three runs were followed by one or two runs in which drifting gratings (in 8 equally spaced directions, at 3 spatial frequencies [0.02, 0.08, and 0.32 cycles per degree]) were presented to the mouse (see below). Stimulus presentation was randomized within each run in each imaging session.

Optogenetic stimulation of $DRN^{5HT \rightarrow dLGN}$ axons in dLGN through the imaging objective (10 s, 15.5 Hz, 8 ms, 2.6 mW, beginning 3 s before stimulus onset and ending 1 s after stimulus offset) was paired with two types of 6-s duration stimuli: a series of stepwise changes in luminance relative to mean luminance (80% contrast, OFF-ON-OFF, 2 s per step; presented for both high (Figure 4–5) and low (Figure 2–3) magnification datasets) and a sequence of 6 adjacent bars (7° x 21° per bar) presented in sequence (1 s duration per bar), with each bar containing a binarized bandpass-filtered spatiotemporal white noise stimulus (spatial frequency corner of 0.05 cycles per degree, a cutoff of 0.32 cycles per degree and a temporal frequency cutoff of 4 Hz; [35], [3], [98], see Supplementary Movie 2; presented only in high magnification imaging sessions [Figure 4–5]) with overall stimulus luminance matched to mean luminance. These bars spanned the area of visual space encoded by boutons in each high magnification FOV. To generate these stimulus movies, we initially measured retinotopy in each FOV, as described below, and identified the two horizontal and two vertical bars that best drove boutons. We then designed the local bar stimulus set to target surrounding retinotopic locations. On subsequent days, we performed experiments pairing optogenetic stimulation with imaging of the same FOV. Stimuli were designed using custom scripts in MATLAB (MathWorks) and presented using NIMH MonkeyLogic. In any one run, 100 trials of each of 5 types were presented in pseudorandom order (each trial lasting 10 seconds, 6 s inter-trial interval): optogenetic stimulation during mean luminance gray screen, presentation of luminance steps with and without optogenetic stimulation, and presentation of localized white noise bars with and without optogenetic stimulation. Recording sessions at low magnification (Figs. 2–3) consisted of two runs of visual stimulation trials (OFF-ON-OFF full-field luminance stimulus) in the presence or absence of optogenetic stimulation and blank trials (mean luminance) in the presence of optogenetic stimulation.

To measure retinotopy, we used a binarized version of a bandpass-filtered noise stimulus with a spatial frequency corner of 0.05 cycles per degree, a cutoff of 0.32 cycles per degree and a temporal frequency cutoff of 4 Hz ([98], [3,35]). Each noise stimulus was contained within a bar, and each bar was presented in a vertical orientation at one of 8 azimuth locations

and in a horizontal orientation at one of 8 elevations, tiling the whole region of visual space covered by the screen (horizontal bars spanned 6° x 74° each, vertical bars spanned 9° x 46° each, Fig. S3A, Supplemental Movie 1). The retinotopy run also included the presentation of a full-field luminance increment and a decrement ('On' or 'Off' trials, respectively, 80% contrast). Both stimulus duration (for all 16 bars and the 2 full-field luminance changes) and inter-stimulus interval lasted 2 s. The responses of boutons to these stimuli were used to define responsiveness inclusion criteria (see below). This allowed for a fair comparison of responses to full-field and local stimuli as they both started from mean luminance. Stimuli were designed using custom scripts in MATLAB (MathWorks) and presented using NIMH MonkeyLogic. Each imaging session included 270 stimulus presentations delivered in pseudorandom order (15 per stimulus type). We did not observe responses to these bars containing white noise in anterior dLGN (Fig S3C). This led us to wonder if boutons in anterior dLGN (many of which showed high baseline activity) were driven bidirectionally by these stimuli, such that the slow nature of calcium signals was averaging out rapid increases and decreases in firing to a net zero change in fluorescence. In a subset of mice, we therefore presented both 8 horizontal and 8 vertical bars containing white noise, and the same bars but containing uniform increases or uniform decreases in luminance (80% luminance contrast). We found that these latter stimuli preferentially drove retinotopic responses in anterior dLGN (Fig S3C).

Drifting grating stimuli were generated and presented using Psychtoolbox (as in [3,35]). We presented full-screen sine-wave drifting gratings (80% contrast) at one of eight directions of motion spaced 45° apart, at spatial frequencies of 0.02, 0.08 and 0.32 cycles per degree and a temporal frequency of 2 Hz. All stimuli were displayed for 2 s. The inter-stimulus interval (mean luminance gray) lasted 2 s.

Slice electrophysiology—We injected AAV2/1.hSyn.FLEX.ChrimsonR-tdTomato virus (Addgene) in the dorsal raphe nucleus of 8 week old Pet1-Cre mice and four weeks later we prepared brain slices for whole-cell patch recording. Brain slices containing the optic tracts and dLGN were prepared as previously described [38]. Briefly, mice were anesthetized using isoflurane (5% in O_2) and perfused with 10 mL of oxygenated (95% O_2; 5% CO_2) ice-cold cutting solution (in mM): 130 K-gluconate, 15 KCl, 0.05 EGTA, 20 HEPES, and 25 glucose (pH 7.4 adjusted with NaOH, 310 mOsm). After decapitation, the brain was removed quickly and immersed in ice-cold cutting solution for one minute. To preserve the integrity of retinogeniculate fibers, parasagittal sectioning was conducted according to the protocol used for the characterization of sensory inputs to the thalamus [99]. The brain was cut with a steel razor blade, then sectioned into 250 μm-thick slices in the oxygenated ice-cold cutting solution using a sapphire blade (Delaware Diamond Knives, Wilmington, DE) on a vibratome (VT1200S; Leica, Deerfield, IL). The slices containing dLGN and optic tracts were recovered at 30°C for 15 minutes in oxygenated saline solution (in mM): 125 NaCl, 26 $NaHCO_3$, 1.25 NaH_2PO_4, 2.5 KCl, 1.0 $MgCl_2$, 2.0 $CaCl_2$, and 25 glucose (pH 7.4, 310 mOsm).

Whole-cell patch clamp recordings were conducted on thalamocortical neurons located in the ventral posterior region of the dLGN. Cells were visualized using a PRIME BSI camera (Teledyne Imaging) connected to a DIC-equipped microscope (Olympus). Glass pipettes

(Drummond Scientific) were pulled on a Sutter p87 Flaming/Brown micropipette puller (Sutter Instruments), and filled with internal solution containing (in mM): 35 CsF, 100 CsCl, 10 EGTA, 10 HEPES, and L-type calcium channel antagonist 0.1 methoxyverapamil (pH 7.4, 300 mOsm). Pipette resistance was 1.5–2.0 MOhm. Patch recordings were performed using a MultiClamp 700B (Axon Instruments), filtered at 1 kHz, and digitized at 4–50 kHz with an ITC-18 interface (Instrutech). Electrically stimulated excitatory post-synaptic currents (eEPSCs) were obtained by impaling saline-filled electrode into optic tracts and stimulating the retinogeniculate inputs. Electrical stimuli were supplied by a stimulus isolator (WPI A365) delivering a 0.2 msec pulse with 100 μA. To obtain AMPA currents, the membrane potential of recorded cells was held at 70 mV, while maintained at 0 mV between trials. Inter-trial intervals were kept at 1 minute. Access resistance was monitored throughout the experiment and evaluated in offline analysis. Experiments with access resistance changing over 20% were removed from analysis. To isolate excitatory synaptic currents, cells were recorded at room temperature in oxygenated saline solution containing 20 μM of bicuculline (antagonist of $GABA_AR$), 10 μM of DPCPX (antagonist of A1 adenosine receptors), 50 μM of LY341495 (blocker of presynaptic mGluRs), and 20 μM of Cyclothiazide (blocker of AMPA desensitization; [100–104]). Offline analysis was conducted using Igor Pro 8 (WaveMetrics) and Matlab (Mathworks, see below).

To stimulate serotonergic terminals in the dLGN, full-field illumination using orange light (> 600 nm) was applied to the slices through a 60x objective (Olympus). The orange light (18 mW) was supplied by a CoolLED pE unit with a 600 nm longpass filter at a frequency of 15 Hz (8 ms pulse width). Orange light stimulation began 500 ms before the first pulse of electrical stimulation of the optic tract and lasted for 600 ms in total. To test the effect of $GABA_BR$ and 5-HT1BR on synaptic transmission, 2 μM of CGP55845 ($GABA_BR$ blocker) and 10 μM of NAS-181 ($5\text{-}HT_{1B}R$ antagonist) were bath applied, respectively.

Perfusion and Immunohistochemistry—We performed immunohistochemistry to examine 5-HT1B expression in a subset of mice. Mice were terminally anesthetized using Avertin (tribromoethanol, 125 mg/kg), and then perfused first with PBS and then with 10% formalin. Brains were extracted and cryopreserved in 20% sucrose before coronal sectioning (40–50 μm thickness). Sections were first blocked in 1% normal donkey serum, 0.1% Triton X-100 in PBS with .05% sodium azide overnight at 4° C, and then incubated in blocking solution containing primary antibodies overnight at 4° C. Sections were washed in PBS, before incubation in blocking solution containing Alexa fluorophore-conjugated secondary antibodies at room temperature for 1.5 hr. Sections were washed in PBS before mounting on slides and imaging with Olympus VS120 slide scanner microscope (Fig. S1) or Zeiss-880 confocal microscope (Fig. 7, S7). We used the following primary antibodies: rabbit anti-5-HT1B (1:500, Abcam, AB13896), guinea pig anti-Vglut2 (1:500, Millipore, AB2251) and chicken anti-GFP (1:1,000, Life Technologies, A10262).

We also performed histology on all mice used in photometry experiments to confirm viral expression of GCaMP6f and ChrimsonR-tdTomato, and fiber placement. Viral expression in two-photon imaging experiments was confirmed *in vivo* via the cranial window.

Confocal imaging—Imaging of immunostained slices (Fig. 7 and Fig. S7) was performed on a Zeiss LSM-880 confocal microscope using 488, 594 and 647 nm excitation wavelengths through a 63x objective. Images were 1024 × 1024 pixels at 15.17 pix/μm, and z-stacks were collected at .37 μm intervals, spanning 5–15 μm.

QUANTIFICATION AND STATISTICAL ANALYSIS

Unless otherwise specified, all analyses were performed using custom scripts in MATLAB (MathWorks).

Analysis of fiber photometry recordings with optogenetic stimulation—Fiber photometry fluorescence signals were collected at 1000 Hz and downsampled to 100 Hz. To ensure no bleedthrough of the 620 nm excitation light used for optogenetic stimulation into the fluorescence recordings, we excluded all timepoints during each 10 ms stimulation pulse from further analysis. The trace was then temporally smoothed by a median filter (width: 100 ms). The change in fluorescence was calculated as $\Delta F/F_0 = (F - F_o)/F_0$, where F_0 is the average fluorescence in the 2 s preceding the onset of a trial. Changes in baseline were measured as the mean ΔF/F between 2 and 3 s after the onset of optogenetic stimulation – after the initial decay in baseline fluorescence and before the onset of visual stimulation. Visual response magnitude was estimated as the mean ΔF/F in the 2 s of visual stimulus presentation. To measure the additional suppression of visual responses by optogenetic stimulation (in addition to the suppression of baseline activity; Fig. S1H and S1P), the visual response amplitude was measured as the difference between the mean ΔF/F during the 2 s of visual stimulus presentation and the mean ΔF/F between 2 and 3 s after the onset of optogenetic stimulation (i.e. the 1-s period prior to visual stimulus onset).

To assess the arousal state of the animal, we tracked changes in pupil area, as in [3]. Due to technical issues, pupil area was measured in 11 of the 12 Pet1-Cre$^{+/-}$ mice reported in Figure 1. To extract the pupil area, we used the same pipeline as described in the section on Two-photon imaging analysis (see below), normalizing the area to the maximal area in each recording session. Arousal state was defined using the mean of the 2 s period before the onset of a trial. To measure the effects of optogenetic stimulation on arousal state, we measured the differences in pupil area and running speed between the 2 s period preceding trial onset and the 4 s window 2–6 s after the onset of optogenetic stimulation on ‘blank’ trials without stimulus presentation (see above). We compared the change in pupil area and running speed on trials with (‘opto’) and trials without (‘ctrl’) optogenetic stimulation. For Fig S1J, trials were only included in which the pupil area during the trial did not vary by more than 1 standard deviation from the mean pupil area in the 2 s preceding the trial onset.

To estimate eye movements during our recordings, we computed the Euclidean x-y displacement of the pupil center of mass. The change in pupil position during optogenetic stimulation (Fig S1K,L,M) was computed as the difference between the average change in pupil position in 2 s before trial onset and in the 2–4 s after onset of optogenetic stimulation. For Figure S1M, trials were only included in which the pupil did not move (less than 1 std. dev. of all changes in pupil position).

Analysis of dual-color fiber photometry recordings—Dual-color photometry data of $GRAB_{5\text{-}HT}$ were analyzed with custom MATLAB scripts, as in [96]. Pulses that trigger the 465-nm and 405-nm LEDs (50 Hz each) were used to determine when the two LEDs were on. To estimate the photometry signal at each LED pulse (6 ms), a median function was applied to the points of the photodetector traces corresponding to the last 3 ms of each pulse. This resulted in two 50 Hz traces: one for the 465-nm channel and another for the 405-nm channel. We corrected for bleaching in each trace by fitting a decaying exponential (as described for time course extraction using two-photon imaging data, below). To calculate the [465 nm–405 nm] trace (termed $GRAB_{5\text{-}HT}$ fluorescence), we first bandpass filtered (as in [105]) the 465-nm and 405-nm traces between .033 and 2 Hz, to avoid overfitting to either fast noise in the signal, or slow components that dominated the 465-nm signal. We then fitted the filtered 405-nm trace to the filtered 465-nm trace using a linear fit, and then scaled and shifted with those coefficients the unfiltered 405-nm trace before subtracting it from the unfiltered 465-nm trace. The scaling was performed separately for each recording session, but resulted in roughly similar coefficients across sessions (not shown). After subtraction, we added back the mean fluorescence of the raw trace such that the mean of the [465 nm–405 nm] trace equalled the mean of the raw 465-nm trace. This allowed for the calculation of ΔF/F for the [465 nm–405 nm] trace using the equation $\Delta F/F_0 = (F - F_0)/F_0$, where F is the fluorescence intensity and F_0 is the mean fluorescence of the whole trace. This procedure allowed us to correct for the particularly strong motion-related signals in the 465-nm fluorescence recordings of $GRAB_{5\text{-}HT}$ (Fig. S5A).

To estimate the amplitude of spontaneous fluctuations in $GRAB_{5\text{-}HT}$ fluorescence (Fig S1E, 5D), we computed the standard deviation of recorded ΔF/F values. To account for variable length of recording sessions (and therefore a potential bias for larger standard deviation in longer sessions), we report the average standard deviation computed over multiple 20-minute segments of each recording session.

Analysis of projection patterns of RGC types in dLGN—To visualize the projections of various retinal ganglion cell types (Fig. S2C-E, S3D), we used data from the Allen Mouse Brain Connectivity Atlas, which provides high-resolution *ex vivo* 3D imaging of fluorescently labeled, genetically-defined cell types. Specifically, we analyzed data from Vglut2-Cre, Kcng4-Cre, and Foxp2-IRES-Cre lines using the Allen Software Development Kit (SDK, https://allensdk.readthedocs.io/_/downloads/en/latest/pdf/) Python code. Vglut2-Cre labels all RGC projections, Kcng4-Cre labels alpha RGC projections, and Foxp2-IRES-Cre labels the F RGC projections [59,69–71]. RGC axons from these lines were visualized by infection with a Cre-dependent fluorescent marker in one eye. The SDK included projection volume data registered to the Common Coordinate Framework (CCF), a 3D average template of the mouse brain [106]. We used the angles of pitch and roll of the headpost relative to the skull (angles from one mouse were used [21° roll, 7° pitch], note: yaw was not used as the animal was head-fixed with the nose pointing forward in the imaging setup) to rotate the 3D matrix containing projection densities to recreate the view of dLGN observed through the cannula during two-photon imaging. To validate this approach, we initially visualized all the RGC axonal projections in the dLGN using Vglut2-Cre. This allowed us to visualize the position of the ipsilateral projections and identify the depth of our

imaging plane (for visualization we averaged a stack of 100 μm, after accounting for tissue compression by the imaging window *in vivo*). To visualize both contralateral and ipsilateral projections, we additionally flipped the 3D volume of Vglut2-Cre inputs along the brain's midline, before applying the rotation to both volumes (Fig S2C-E). To characterize the innervation patterns of Kcng4-Cre and Foxp2-Cre RGCs throughout the dLGN, we averaged the volume data for 3 experiments in each line. By overlaying the expression profiles from Foxp2-Cre and Kcng4-Cre, we could compare these projections of F and alpha RGCs, respectively, to the spatial distribution of functional categories of RGC boutons in *in vivo* the two-photon calcium imaging data. With this visualization we observed spatial segregation of Kcng4-Cre and Foxp2-Cre along the anterior-posterior axis of the dorsolateral surface of the dLGN. This, together with our tilt in pitch, suggests that the anterior part of our FOV might be grazing the dorsal edge of the 'core' of dLGN, while the posterior part of our FOV might be sampling from the 'shell', which is known to be thicker in posterior dLGN [59,107].

Analysis of scSeq data—For analysis of *htr1b* expression in RGCs shown in Fig 7H and S7I, transcriptomic data of 35,699 adult RGCs classified into 45 molecular clusters was obtained from: https://singlecell.broadinstitute.org/single_cell/study/SCP509/mouse-retinal-ganglion-cell-adult-atlas-and-optic-nerve-crush-time-series [33].

Analysis of whole-mount retina electrophysiology—Data from whole-cell electrophysiology recordings in whole mount retina were obtained from RGCtypes.org [32]. For each cell, we assessed baseline firing (Figure S7K) as the firing in the 1 s in darkness preceding presentation of a white spot, averaged across trials of all spot sizes. The response amplitude to spots of different sizes was calculated as the average firing in the 250 ms following the onset (for 'ON' cells) and the offset (for 'OFF' cells) of the spot presentation. To obtain spot-size tuning curves for each cell type (Fig. S7J *left*), we baseline subtracted and peak-normalized the averaged response of all cells of a type. The preference of a cell for large vs. small spots (Fig. S7J *middle*) was calculated as $(R_2 - R_1)/(R_2 + R_1)$, where R2 is a cell's average response to spots with a diameter greater than 800 μm (approximately 26° of visual space) and R1 is a cell's average response to spots smaller than 150 μm in diameter (approximately 5° of visual space).

Analysis of confocal imaging—To measure 5-HT1B receptor expression on RGC boutons of different types, we first identified RGC boutons using morphological image segmentation of 3D images of Vglut2 expression (labeling all RGC presynaptic terminals) and of YFP expression (labeling axons of Cre-expressing RGCs infected with a Cre-dependent fluorescent marker, see 'Virus Injections' above). We smoothed the data with a 3D median filter before removing background using morphological 'opening' and 'closing' with a 4 μm diameter disk-shaped structuring element and 3D Gaussian filtering. Images were then binarized to identify Vglut2-enriched or YFP- and Vglut2-enriched areas corresponding to presynaptic terminals of all RGCs or of a specific subtype. Masks were only included if they had a diameter of at least .75 μm. For each mask, we then calculated the average 5-HT1B receptor antibody staining intensity. To assess differences in 5-HT1B intensity in YFP-expressing axon terminals across slices, we compared 5-HT1B intensity in YFP-enriched terminals to the intensity in Vglut2-enriched terminals in each slice. This

allowed us to compare intensity in different subsets of RGCs vs. all RGCs without the confound of overall differences in 5-HT1B staining in different slices.

Analysis of whole-cell patch recordings in dLGN—In order to measure the effects of $DRN^{5HT \rightarrow dLGN}$ photostimulation on glutamate release, we measured the peak amplitude of AMPAR-mediated excitatory post-synaptic currents (EPSCs) evoked by electrical stimulation of the optic tract in the presence or absence of $DRN^{5HT \rightarrow dLGN}$ photostimulation. The percent suppression during trials with optogenetic stimulation was calculated as

$$\% \ suppression = \frac{EPSC_{ctrl} - EPSC_{opto}}{EPSC_{ctrl}} \times 100$$

Where $EPSC_{opto}$ was the amplitude of the EPSC on trials with optogenetic stimulation, and $EPSC_{ctrl}$ was the average amplitude of the EPSC on the five trials preceding the trial with optogenetic stimulation. In order to assess the effect of bath-applied drugs on suppression of glutamate release by $DRN^{5HT \rightarrow dLGN}$ photostimulation, the percent suppression by photostimulation for each cell before and after bath application of drugs was considered.

Two-photon imaging analysis

Image registration and timecourse extraction: To correct for x-y shifts in the FOV due to motion, image registration was performed in a manner similar to our prior studies [3,35]. Briefly, the fluorescence movie for each run was first registered to a common average field-of-view using efficient rigid-body subpixel registration methods (on average this led to correction of motion of 1.5 μm in X and .5 μm in Y; no change in average motion was observed during optogenetic stimulation). The registered movies were then spatially downsampled by 2 and temporally downsampled by 15. For registration purposes only, a local image normalization method (http://bigwww.epfl.ch/sage/soft/localnormalization/) was applied to each frame to normalize the fluorescence intensity across boutons and to increase the contrast between boutons and neuropil. After normalization, image warping using the imregdemons.m function (MATLAB) was implemented to align all images to a new common average field of view. The pixel-wise displacement resulting from the imregdemons function was spatially and temporally upsampled and then applied to the original, subpixel-registered movies. A second round of image warping was then applied to the full-sized, processed movies. The resulting estimate of pixel-wise displacements was then applied to the aligned movies from the first round of image warping. After these image registration and warping steps, no obvious x-y motion was observed and PCA de-noising was performed (using PCs with eigenvalues above those of a random matrix [108]).

Finally, movies from sequential runs were aligned to the movie of the first run in two steps. First, we evaluated the rigid-body displacement between the average image from each movie and the first movie of each session and applied that to each frame. Next, we evaluated local warping using the imregdemons.m function applied to the average image from each movie and the average image of the first movie of each session and applied the displacement field to each frame of the movies.

After image registration, regions of interest were identified using Suite2p [109] which provided weighted masks for individual boutons and neuropil masks. The fluorescence intensity at each timepoint for a given bouton and its associated neuropil mask is given as the weighted average of the fluorescence intensities across pixels in the mask.

To account for photobleaching during imaging sessions, a bleaching correction method was implemented [3,35]. Raw bouton and neuropil traces were first smoothed using a sliding filter (30th percentile of a 5-minute sliding window). Then, the filtered traces were fitted using a decaying exponential,

$$a \times e^{-x/\tau} + b$$

where the amplitude (a) and the offset (b) were independently estimated for each bouton and each neuropil ring, while the time constant (τ) was fixed to an empirically defined constant value of 75 minutes.

To correct for photobleaching in each trace, we subtracted the offset, before dividing by the exponential decay. Lastly, we added back the offset.

To account for neuropil signals which may contaminate signals in the bouton trace, neuropil correction was applied by subtracting a scaled version of the corresponding neuropil trace (0.6 x neuropil trace) from each bouton trace before adding back the mean neuropil fluorescence (temporally-averaged across the neuropil trace [110]).

Finally, fractional change in fluorescence on each trial was calculated as $\Delta F/F_0 = (F - F_o)/F_0$. For trials in which we presented drifting sinusoidal gratings or retinotopy bars, F_0 is the mean fluorescence in the second preceding onset of the visual stimulus. For imaging runs in which we paired optogenetic stimulation with the presentation of visual stimuli, F_0 is the mean fluorescence in the 2 s preceding trial onset (where each trial starts with 3 s of mean luminance gray screen which on half the trials is paired with optogenetic stimulation, followed by the onset of a 6 s visual stimulus).

Bouton selection (QI): All analyses were performed on driven boutons, defined as regions of interest (ROIs) that passed the following inclusion criteria. A quality index was computed for each type of trial, as in [34]

$$QI = \frac{Var[\langle C \rangle_r]_t}{\langle Var[C]_t \rangle_r}$$

where C is the response matrix (time x trials) and $\langle\ \rangle_x$ and $Var[\ ]_x$ denote the mean and variance (across either trials [r] or timepoints [t]). For low-magnification imaging sessions that spanned the whole surface of dLGN (Figs. 2–3), a bouton was included in further analysis if it (i) had a QI greater than .15 on at least one of two types of full-field trials (2 s of luminance increments or decrements) or (ii) had a QI greater than .15 in response to at least one horizontal and one vertical whitenoise bar (see above for description of stimuli). For imaging sessions using higher magnification (Figs. 4–5), boutons additionally

had to have a QI greater than .15 in response to either of the two visual stimuli that were paired with optogenetic stimulation (6 s luminance step or spatially localized sequence of bars containing white noise, see above). The fixed threshold of .15 for QI was established empirically, based on inspection of individual bouton response traces. Varying the threshold did not qualitatively impact our results. FOV analyses (Fig. 4G and S4E-F) were performed on FOVs with at least 5% each of Bar and FF boutons.

Bouton classification: For imaging sessions at lower magnification that spanned the whole surface of dLGN (Fig. 2–3), driven boutons were classified into 1 of 4 categories based on their responses to full-field luminance changes (‘full-field stimuli’, 2 s of luminance increment or decrement) and horizontal or vertical bars of whitenoise (‘retinotopy bar’). A ‘FF’ bouton was defined as a bouton that had a QI greater than .15 in response to at least one of the two types of full-field stimuli but did not have a QI greater than .15 in response to any horizontal and or vertical retinotopy bar. A ‘FF+Bar’ bouton had a QI greater than .15 for both types of stimuli. A ‘Bar’ bouton had a QI greater than .15 in response to at least one horizontal and one vertical retinotopy bar, but not to any of the full-field stimuli. A bouton was defined as suppressed by contrast (‘SBC’) if it had a QI greater than .15 in response to at least one horizontal and one vertical retinotopy bar, but was not activated (increases in $\Delta F/F$) by any retinotopy bar (the combination of these criteria indicated reliable suppression by retinotopy bar).

For imaging sessions using higher magnification (Fig. 4), the QI on trials of full-field stepwise luminance changes (‘step stimuli’) and of 6 s sequence of localized white-noise bars (‘local bars’, the stimuli paired with optogenetic stimulation) was used as an additional criterion for assigning boutons to categories. FF boutons had a QI greater than .15 in response to full-field stimuli and step stimuli, but not in response to retinotopy bars or local bars. Bar boutons had a QI greater than .15 in response to local bars and at least one horizontal and one vertical retinotopy bar, but not in response to full-field or step stimuli. FF+Bar boutons had a QI greater than .15 in response to all four stimulus types. SBC boutons were defined using their QI in response to both retinotopy bars and drifting gratings. They had a QI greater than .15 in response to at least one horizontal, one vertical retinotopy bar and one drifting grating, but were not activated (increases in $\Delta F/F$) by any retinotopy bar or drifting grating (the combination of these criteria indicated reliable suppression by retinotopy bars and drifting gratings).

Pupil data analysis: To assess the arousal state of the animal we tracked changes in pupil area, as in [3]. To extract the pupil area, morphological filters and the grayconnected.m function (MATLAB, MathWorks) were used to identify the region of the image that belonged to the pupil. The regionprops.m function (MATLAB, Mathworks) was then used to fit an ellipse to the pupil region and to measure parameters of the ellipse, including the centroid position, the width, and the height. Pupil area was calculated as the area of the fitted ellipse, normalized to the maximal pupil area during each session, and temporally smoothed by a median filter (width: 5 adjacent frames/330 ms). The pupil area on each trial was defined as the mean pupil area in the two seconds before trial onset (trial onset defined as 3 s before visual stimulus- the time at which the optogenetic stimulus begins). For

analyses in Fig. 5E-H and Fig. S5G-I, the visual response during high or low arousal trials was defined as the mean response across trials without optogenetic stimulation where the pupil was respectively greater or less than 50% of the maximum pupil area on that session. Boutons from a given recording were included in this analysis only if the recording had at least 5 trials at high and 5 at low arousal. For analyses in Fig. S5G effects of optogenetic stimulation were assessed using control and optogenetic trials with pre-trial pupil area in the same range.

Baseline suppression and baseline level: During imaging runs and photometry recording sessions in which visual stimulation was paired with optogenetic stimulation of $DRN^{5HT \rightarrow dLGN}$ axons, all trials began with a 3 s period of baseline during which the mouse was looking at a mean luminance grey screen (the same as during the inter-trial periods). On half of the trials optogenetic stimulation was delivered in this period. On a subset of 'blank' trials optogenetic stimulation was presented (for 10 s during two-photon imaging, for 6 s during photometry recordings) while the mouse was looking at a mean luminance grey screen. Baseline suppression by $DRN^{5HT \rightarrow dLGN}$ photostimulation was measured as the mean fractional change in fluorescence ($\Delta F/F$) in a 1 s period starting 2 s after the onset of optogenetic stimulation (where F_0 was the average fluorescence in the 2 s before optogenetic stimulation, see above). We restricted the measurement to this period to allow the fluorescence to decay during $DRN^{5HT \rightarrow dLGN}$ photostimulation and reach a new steady state.

The baseline level of each bouton was assessed as the mean value of the 1 s period preceding visual stimulus onset on trials without optogenetic stimulation, normalized to the dynamic range of the bouton (see below).

Morphological alignment of dLGN surface: In Figs. 2G, S2A,B,H and S3C,E,F, we show the spatial distribution (i) of baseline suppression by $DRN^{5HT \rightarrow dLGN}$ stimulation across functional categories and (ii) of retinotopic responses pooled across all 6 mice. To achieve this pooling, we performed a morphological alignment of each low magnification FOV, which in each mouse encompassed the entire dorsolateral surface of dLGN. First, for each mouse we manually defined the contour of dLGN defined by the presence of GCaMP fluorescence and based on the area of the FOV in which we observed responses to full-field luminance increments or decrements or bars of binarized white-noise (see for example Fig. 2C, Supplementary Movie 1). Next, we considered the FOV from the first imaged mouse as the reference image and used the function imregtform.m (MathWorks) to estimate the rigid-body transformation between the reference image and the outline of the dLGN in all other mice. The displacements were then applied to the X-Y coordinates for the centroid of each bouton's mask (as defined by Suite2p during bouton identification). This across-mouse registration based on GCaMP fluorescence was then applied to the images of the ipsilateral RGC projection infected with CTB-A647. The mean of the GCaMP and A647 images from 4 mice is shown in Fig. S2B, illustrating the consistency of our imaging FOV along the dorsolateral surface of dLGN.

Dynamic range: To compute the dynamic range of each bouton, we considered the 20^{th} and 80^{th} percentile of response amplitudes to each trial type (including baseline periods,

but excluding optogenetic trials). The minimum of the 20th percentile response amplitudes across trial types, and the maximum of the 80th percentile response amplitudes across trial types, were considered the bottom and top of the dynamic range, respectively. The reason we used the 20th and 80th percentile of response amplitudes (instead of the minimum and maximum) to each trial type was in order to conservatively estimate the true dynamic range of the response amplitudes without accounting for nonbiological noise sources like shot noise. For imaging sessions that spanned the whole surface of dLGN (Figs. 2–3), the trial types used in estimating this global minimum and maximum were those involving each of the 8 horizontal and 8 vertical bars, the 2 s luminance increment and decrement trials and the 6 s stepwise luminance change trials. For imaging sessions using higher magnification (Figs. 4–5), we additionally included trials (without optogenetic stimulation) that involved the 6-s luminance steps (considering each 2-s portion with a luminance increase or decrease separately) and the trials with 6 1-s presentations of bars containing white noise in nearby regions of space (considering each 1-s portion separately), as well as trials involving sinusoidal drifting gratings in one of 8 directions, presented at one of 3 spatial frequencies.

Spatial Frequency preference: To compute an index related to spatial frequency preference, we computed a weighted sum of the responses of each bouton to drifting gratings presented at each of three spatial frequencies (.02, .08 and .32 cycles per degree [cpd], similar to [3]). As drifting gratings were presented moving in 8 directions, for each spatial frequency the response used was that for the direction that elicited the maximal response. For SBC boutons, we inverted the sign of the response at each spatial frequency. The weighted sum was given by the formula

$$SF_{pref} = \frac{R_{SF1} + 2 * R_{SF2} + 3 * R_{SF3}}{R_{SF1} + R_{SF2} + R_{SF3}}$$

Where R_{SF1}, R_{SF2} and R_{SF3} are the responses to drifting gratings at .02, .08 and .32 cycles per degree, respectively. The analyses in Fig. 4H (comparing spatial frequency preference to suppression by DRN$^{5HT\rightarrow dLGN}$ photostimulation) were restricted to FF+Bar boutons that had a QI greater than .15 in response to at least one drifting grating moving in one direction at one spatial frequency.

Retinotopic preference: Retinotopic preference of each bouton along the azimuth and elevation axes was computed as in [35], using either elongated bars containing white noise (Fig. S3E$_1$, S4B-C), or uniformly dark or bright bars. For the latter dataset involving uniformly dark or bright bars, we took the average of the absolute values of the responses to the presentations of bright and dark bar at each given location (Fig. S3E$_2$). For retinotopic tuning curve fitting, this produced two curves of eight evenly spaced values, which were approximated using a Gaussian function:

$$R(x) = R_1 e^{-\frac{(x - x_{pref})^2}{2\sigma^2}} + R_{off}$$

The fitted ΔF/F response, R(x), varied as a function of the retinotopic stimulus location, x. The maximum response, R1 + R off, was evoked at x$_{pref}$, the preferred retinotopic location.

To increase the number of points for fitting from 8 to 15, an interpolation method similar to the one used for direction tuning curves was implemented. Retinotopic preference was only considered for boutons that had QI > .15 in response to at least one horizontal and one vertical bar.

Axis and direction selectivity: As in [35], for each bouton, we calculated a 'vector sum' axis selectivity index (ASI; i.e., selectivity for motion along a given axis) on each interpolated direction tuning curve[110]. This index was calculated by projecting the ΔF/F response (R) for each of the 8 directions (θ, interpolated to 16 points) in the range between 0° and 360° onto a circle with 2i progression and estimating the magnitude of the normalized vector sum, which ranged from 0 to 1 (maximum selectivity):

$$ASI = \left| \sum_{n=1}^{16} R(\theta_n) e^{2i * \frac{2\pi\theta_n}{360°}} \right| / \sum_{n=1}^{16} |R(\theta_n)|$$

Opposite directions contributed in an additive fashion, while orthogonal directions canceled each other out. In a similar manner, we computed a 'vector sum' direction selectivity index (DSI), by projecting the 8 directions (interpolated to 16 points) onto a circle with 1i progression:

$$DSI = \left| \sum_{n=1}^{16} R(\theta_n) e^{1i * \frac{2\pi\theta_n}{360°}} \right| / \sum_{n=1}^{16} |R(\theta_n)|$$

To obtain a ASI and DSI estimate for a given bouton (Fig. S4H), the ASI and DSI at the preferred spatial frequency were used.

On-Off index: The preference of boutons for increases vs. decreases in luminance was calculated as in [35]. An On-Off index was calculated as follows:

$$OnOff\ index = \frac{(On_R - Off_R) \cdot (|On_R| + |Off_R|)}{\| |On_R| + |Off_R| \|^2}$$

On_R and Off_R were defined as the ON and OFF response time courses during the 2 s response window (the stimuli used were 2 s full-field increments or decrements in luminance starting from a mean luminance gray screen). A positive response to increments (ON) only, to decrements (OFF) only, or a positive response of equal magnitude to increments and decrements (ON and OFF) corresponded to index values of 1, −1 or 0, respectively. For quantifications in Fig. S5K-L, ON boutons were defined as having an On-Off index greater than .9 and OFF boutons were defined as having an On-Off index less than −.9.

DRN axon masks: To estimate the density of DRN axons around each RGC bouton, we first summed a z-stack of DRN axon from 5 μm below to 5 μm above the imaging plane (sampled at 5 μm intervals). We used morphological filtering and thresholding to binarize the resulting fluorescence image of DRN axons, thereby generating DRN axon masks. We then calculated

the fraction of pixels, in a disc of 10 μm radius around the RGC bouton's center of mass, that belonged to a DRN axon mask.

Statistics—Statistical tests were performed using MATLAB (MathWorks). Additional details on sample sizes and statistical test for each experiment can be found in figure legends and main text. To account for dependencies originating from nesting in some of our data (multiple cells from individual animals, or repeated recording sessions from individual animals), we tested for significance of these results by fitting linear mixed effects models (using 'fitlme' in MATLAB, MathWorks). We fit two types of models. The first was used to model whether a distribution was significantly different from zero ('intercept'), while accounting for repeated measures from the same mouse ('random effects'). We used the formula: y ~ 1 + (1|Mouse), where y is a vector of observations. We used this model on data in Figures 1C–1E, 1H, 1I, 1N, 2E, S1C, S1H, S1J, S1K, S1M, S1P, and S5E. The second model was used to compare the effects between RGC types ('fixed effects'), while accounting for multiple cells recorded from the same mouse ('random effects'). We used the formula: y ~ 1 + Type + (1|Mouse), where y is a vector of observations. We used this model on data in Fig 3C–3E, 3G, 4F, 5F, S4D, S5G, and S5J-L. Significance levels are indicated as follows: *p < 0.05; **p < 0.01; ***p < 0.001. Experiments were conducted by an investigator with knowledge of the animal genotype and treatment. Virus expression and optic fiber implant placements were verified by post hoc histology. Viral expression in two-photon imaging experiments was confirmed *in vivo* via the cranial window.

Supplementary Material

Refer to Web version on PubMed Central for supplementary material.

Acknowledgements

We thank G. Schwartz, S. Zhang, A. Landau, J. Sanes, A. Fratzl, H. Acaron, J.S. Alvarado, and members of the Chen and Andermann lab for helpful discussion and feedback. We thank R. Essner, K. Fernando, C. Welsh and I. D'Alessandro for experimental assistance. We thank Drs. Jayaraman, Kerr, Kim, Looger, and Svoboda and the GENIE Project, Janelia Farm Research Campus, HHMI, for GCaMP6. We thank the Boston Children's Hospital viral core (supported by NIH P30 EY012196) for virus packaging and the IDDRC Cellular Imaging Core (supported by U54 HD090255). Support was provided by a Simons Collaboration on the Global Brain Postdoctoral Fellowship (to L.L.), NIH R01EY013613 (to C.C.), the Harvard/MIT Joint Research Grants Program in Basic Neuroscience and NIH R21 EY030243 and R01 EY032749 (to C.C. and M.L.A.), an NIH DP2DK105570, R01 DK109930, DP1 AT010971, and grants from the Smith Family Foundation, the Pew Scholars Program in the Biomedical Sciences (to M.L.A.).

REFERENCES

1. Sherman SM (2005). The role of the thalamus in cortical function: not just a simple relay. Thalamus & Related Systems 3, 205–216.
2. Coen-Cagli R, Kanitscheider I, and Pouget A (2017). A method to estimate the number of neurons supporting visual orientation discrimination in primates. F1000Res 6, 1752. 10.12688/f1000research.12398.1. [PubMed: 29333238]
3. Liang L, Fratzl A, Reggiani JDS, El Mansour O, Chen C, and Andermann ML (2020). Retinal Inputs to the Thalamus Are Selectively Gated by Arousal. Curr Biol 30, 3923–3934 e3929. 10.1016/j.cub.2020.07.065. [PubMed: 32795442]

4. Schroder S, Steinmetz NA, Krumin M, Pachitariu M, Rizzi M, Lagnado L, Harris KD, and Carandini M (2020). Arousal Modulates Retinal Output. Neuron 107, 487–495 e489. 10.1016/j.neuron.2020.04.026. [PubMed: 32445624]
5. Aydin C, Couto J, Giugliano M, Farrow K, and Bonin V (2018). Locomotion modulates specific functional cell types in the mouse visual thalamus. Nat Commun 9, 4882. 10.1038/s41467-018-06780-3. [PubMed: 30451819]
6. Erisken S, Vaiceliunaite A, Jurjut O, Fiorini M, Katzner S, and Busse L (2014). Effects of locomotion extend throughout the mouse early visual system. Curr Biol 24, 2899–2907. 10.1016/j.cub.2014.10.045. [PubMed: 25484299]
7. Roth MM, Dahmen JC, Muir DR, Imhof F, Martini FJ, and Hofer SB (2016). Thalamic nuclei convey diverse contextual information to layer 1 of visual cortex. Nat Neurosci 19, 299–307. 10.1038/nn.4197. [PubMed: 26691828]
8. Nestvogel DB, and McCormick DA (2022). Visual thalamocortical mechanisms of waking state-dependent activity and alpha oscillations. Neuron 110, 120–138 e124.10.1016/j.neuron.2021.10.005. [PubMed: 34687663]
9. Crombie D, Spacek MA, Leibold C, Busse L (2021). Pupil size dynamics predict dLGN firing mode over a wide range of timescales. bioRxiv 2021.*04.30.442134*.
10. Niell CM, and Stryker MP (2010). Modulation of visual responses by behavioral state in mouse visual cortex. Neuron 65, 472–479. 10.1016/j.neuron.2010.01.033. [PubMed: 20188652]
11. Andermann ML, Kerlin AM, Roumis DK, Glickfeld LL, and Reid RC (2011).Functional specialization of mouse higher visual cortical areas. Neuron 72, 1025–1039. 10.1016/j.neuron.2011.11.013. [PubMed: 22196337]
12. Dipoppa M, Ranson A, Krumin M, Pachitariu M, Carandini M, and Harris KD (2018). Vision and Locomotion Shape the Interactions between Neuron Types in Mouse Visual Cortex. Neuron 98, 602–615 e608. 10.1016/j.neuron.2018.03.037. [PubMed: 29656873]
13. Williamson RS, Hancock KE, Shinn-Cunningham BG, and Polley DB (2015). Locomotion and Task Demands Differentially Modulate Thalamic Audiovisual Processing during Active Search. Curr Biol 25, 1885–1891. 10.1016/j.cub.2015.05.045. [PubMed: 26119749]
14. McGinley MJ, Vinck M, Reimer J, Batista-Brito R, Zagha E, Cadwell CR, Tolias AS, Cardin JA, and McCormick DA (2015). Waking State: Rapid Variations Modulate Neural and Behavioral Responses. Neuron 87, 1143–1161. 10.1016/j.neuron.2015.09.012. [PubMed: 26402600]
15. Vinck M, Batista-Brito R, Knoblich U, and Cardin JA (2015). Arousal and locomotion make distinct contributions to cortical activity patterns and visual encoding. Neuron 86, 740–754. 10.1016/j.neuron.2015.03.028. [PubMed: 25892300]
16. Neske GT, Nestvogel D, Steffan PJ, and McCormick DA (2019). Distinct Waking States for Strong Evoked Responses in Primary Visual Cortex and Optimal Visual Detection Performance. J Neurosci 39, 10044–10059. 10.1523/JNEUROSCI.1226-18.2019. [PubMed: 31672787]
17. Joshi S, and Gold JI (2020). Pupil Size as a Window on Neural Substrates of Cognition. Trends Cogn Sci 24, 466–480. 10.1016/j.tics.2020.03.005. [PubMed: 32331857]
18. Larsen RS, and Waters J (2018). Neuromodulatory Correlates of Pupil Dilation. Front Neural Circuits 12, 21. 10.3389/fncir.2018.00021. [PubMed: 29593504]
19. Reimer J, McGinley MJ, Liu Y, Rodenkirch C, Wang Q, McCormick DA, and Tolias AS (2016). Pupil fluctuations track rapid changes in adrenergic and cholinergic activity in cortex. Nat Commun 7, 13289. 10.1038/ncomms13289. [PubMed: 27824036]
20. Nelson A, and Mooney R (2016). The Basal Forebrain and Motor Cortex Provide Convergent yet Distinct Movement-Related Inputs to the Auditory Cortex. Neuron 90, 635–648. 10.1016/j.neuron.2016.03.031. [PubMed: 27112494]
21. Fitzpatrick D, Diamond IT, and Raczkowski D (1989). Cholinergic and monoaminergic innervation of the cat's thalamus: comparison of the lateral geniculate nucleus with other principal sensory nuclei. J Comp Neurol 288, 647–675. 10.1002/cne.902880411. [PubMed: 2478594]
22. Seo C, Guru A, Jin M, Ito B, Sleezer BJ, Ho YY, Wang E, Boada C, Krupa NA, Kullakanda DS, et al. (2019). Intense threat switches dorsal raphe serotonin neurons to a paradoxical operational mode. Science 363, 538–542. 10.1126/science.aau8722. [PubMed: 30705194]

23. Paquelet GE, Carrion K, Lacefield CO, Zhou P, Hen R, and Miller BR (2022). Single-cell activity and network properties of dorsal raphe nucleus serotonin neurons during emotionally salient behaviors. Neuron 110, 2664–2679 e2668. 10.1016/j.neuron.2022.05.015. [PubMed: 35700737]
24. Michaiel AM, Parker PRL, and Niell CM (2019). A Hallucinogenic Serotonin-2A Receptor Agonist Reduces Visual Response Gain and Alters Temporal Dynamics in Mouse V1. Cell Rep 26, 3475–3483 e3474. 10.1016/j.celrep.2019.02.104. [PubMed: 30917304]
25. Lottem E, Banerjee D, Vertechi P, Sarra D, Lohuis MO, and Mainen ZF (2018). Activation of serotonin neurons promotes active persistence in a probabilistic foraging task. Nat Commun 9, 1000. 10.1038/s41467-018-03438-y. [PubMed: 29520000]
26. Seillier L, Lorenz C, Kawaguchi K, Ott T, Nieder A, Pourriahi P, and Nienborg H (2017). Serotonin Decreases the Gain of Visual Responses in Awake Macaque V1. J Neurosci 37, 11390–11405. 10.1523/JNEUROSCI.1339-17.2017. [PubMed: 29042433]
27. Fu Y, Kaneko M, Tang Y, Alvarez-Buylla A, and Stryker MP (2015). A cortical disinhibitory circuit for enhancing adult plasticity. Elife 4, e05558. 10.7554/eLife.05558.
28. Monckton JE, and McCormick DA (2002). Neuromodulatory role of serotonin in the ferret thalamus. J Neurophysiol 87, 2124–2136. 10.1152/jn.00650.2001. [PubMed: 11929930]
29. McCormick DA, and Pape HC (1990). Noradrenergic and serotonergic modulation of a hyperpolarization-activated cation current in thalamic relay neurones. J Physiol 431, 319–342. 10.1113/jphysiol.1990.sp018332. [PubMed: 1712844]
30. Gil Z, Connors BW, and Amitai Y (1997). Differential regulation of neocortical synapses by neuromodulators and activity. Neuron 19, 679–686. 10.1016/s08966273(00)80380-3. [PubMed: 9331357]
31. Sanes JR, and Masland RH (2015). The types of retinal ganglion cells: current status and implications for neuronal classification. Annu Rev Neurosci 38, 221–246. 10.1146/annurev-neuro-071714-034120. [PubMed: 25897874]
32. Goetz J, Jessen ZF, Jacobi A, Mani A, Cooler S, Greer D, Kadri S, Segal J, Shekhar K, Sanes JR, and Schwartz GW (2022). Unified classification of mouse retinal ganglion cells using function, morphology, and gene expression. Cell Rep 40, 111040. 10.1016/j.celrep.2022.111040.
33. Tran NM, Shekhar K, Whitney IE, Jacobi A, Benhar I, Hong G, Yan W, Adiconis X, Arnold ME, Lee JM, et al. (2019). Single-Cell Profiles of Retinal Ganglion Cells Differing in Resilience to Injury Reveal Neuroprotective Genes. Neuron 104, 1039–1055 e1012. 10.1016/j.neuron.2019.11.006. [PubMed: 31784286]
34. Baden T, Berens P, Franke K, Roman Roson M, Bethge M, and Euler T (2016). The functional diversity of retinal ganglion cells in the mouse. Nature 529, 345–350. 10.1038/nature16468. [PubMed: 26735013]
35. Liang L, Fratzl A, Goldey G, Ramesh RN, Sugden AU, Morgan JL, Chen C, and Andermann ML (2018). A Fine-Scale Functional Logic to Convergence from Retina to Thalamus. Cell 173, 1343–1355 e1324. 10.1016/j.cell.2018.04.041. [PubMed: 29856953]
36. Rompani SB, Mullner FE, Wanner A, Zhang C, Roth CN, Yonehara K, and Roska B (2017). Different Modes of Visual Integration in the Lateral Geniculate Nucleus Revealed by Single-Cell-Initiated Transsynaptic Tracing. Neuron 93, 767–776 e766. 10.1016/j.neuron.2017.01.028. [PubMed: 28231464]
37. Roman Roson M, Bauer Y, Kotkat AH, Berens P, Euler T, and Busse L (2019). Mouse dLGN Receives Functional Input from a Diverse Population of Retinal Ganglion Cells with Limited Convergence. Neuron 102, 462–476 e468. 10.1016/j.neuron.2019.01.040. [PubMed: 30799020]
38. Litvina EY, and Chen C (2017). Functional Convergence at the Retinogeniculate Synapse. Neuron 96, 330–338 e335. 10.1016/j.neuron.2017.09.037. [PubMed: 29024658]
39. Morgan JL, Berger DR, Wetzel AW, and Lichtman JW (2016). The Fuzzy Logic of Network Connectivity in Mouse Visual Thalamus. Cell 165, 192–206. 10.1016/j.cell.2016.02.033. [PubMed: 27015312]
40. Chen C, and Regehr WG (2003). Presynaptic modulation of the retinogeniculate synapse. J Neurosci 23, 3130–3135. [PubMed: 12716920]

41. Seeburg DP, Liu X, and Chen C (2004). Frequency-dependent modulation of retinogeniculate transmission by serotonin. J Neurosci 24, 10950–10962. 10.1523/JNEUROSCI.3749-04.2004. [PubMed: 15574745]
42. Pickard GE, Smith BN, Belenky M, Rea MA, Dudek FE, and Sollars PJ (1999). 5-HT1B receptor-mediated presynaptic inhibition of retinal input to the suprachiasmatic nucleus. J Neurosci 19, 4034–4045. [PubMed: 10234032]
43. Smith BN, Sollars PJ, Dudek FE, and Pickard GE (2001). Serotonergic modulation of retinal input to the mouse suprachiasmatic nucleus mediated by 5-HT1B and 5-HT7 receptors. J Biol Rhythms 16, 25–38. 10.1177/074873040101600104. [PubMed: 11220775]
44. Mooney RD, Huang X, Shi MY, Bennett-Clarke CA, and Rhoades RW (1996). Serotonin modulates retinotectal and corticotectal convergence in the superior colliculus. Prog Brain Res 112, 57–69. 10.1016/s0079-6123(08)63320-8. [PubMed: 8979820]
45. Petzold GC, Hagiwara A, and Murthy VN (2009). Serotonergic modulation of odor input to the mammalian olfactory bulb. Nat Neurosci 12, 784–791. 10.1038/nn.2335. [PubMed: 19430472]
46. Fitzgerald KK, and Sanes DH (1999). Serotonergic modulation of synapses in the developing gerbil lateral superior olive. J Neurophysiol 81, 2743–2752. 10.1152/jn.1999.81.6.2743. [PubMed: 10368394]
47. Lutas A, Kucukdereli H, Alturkistani O, Carty C, Sugden AU, Fernando K, Diaz V, Flores-Maldonado V, and Andermann ML (2019). State-specific gating of salient cues by midbrain dopaminergic input to basal amygdala. Nat Neurosci 22, 1820–1833. 10.1038/s41593-019-0506-0. [PubMed: 31611706]
48. Wan J, Peng W, Li X, Qian T, Song K, Zeng J, Deng F, Hao S, Feng J, Zhang P, et al. (2021). A genetically encoded sensor for measuring serotonin dynamics. Nat Neurosci 24, 746–752. 10.1038/s41593-021-00823-7. [PubMed: 33821000]
49. Cazettes F, Reato D, Morais JP, Renart A, and Mainen ZF (2021). Phasic Activation of Dorsal Raphe Serotonergic Neurons Increases Pupil Size. Curr Biol 31, 192–197 e194. 10.1016/j.cub.2020.09.090. [PubMed: 33186549]
50. Oikonomou G, Altermatt M, Zhang RW, Coughlin GM, Montz C, Gradinaru V, and Prober DA (2019). The Serotonergic Raphe Promote Sleep in Zebrafish and Mice. Neuron 103, 686–701 e688. 10.1016/j.neuron.2019.05.038. [PubMed: 31248729]
51. Hooks BM, and Chen C (2006). Distinct roles for spontaneous and visual activity in remodeling of the retinogeniculate synapse. Neuron 52, 281–291. 10.1016/j.neuron.2006.07.007. [PubMed: 17046691]
52. Chen C, Blitz DM, and Regehr WG (2002). Contributions of receptor desensitization and saturation to plasticity at the retinogeniculate synapse. Neuron 33, 779–788. 10.1016/s0896-6273(02)00611-6. [PubMed: 11879654]
53. Marvin JS, Scholl B, Wilson DE, Podgorski K, Kazemipour A, Muller JA, Schoch S, Quiroz FJU, Rebola N, Bao H, et al. (2018). Stability, affinity, and chromatic variants of the glutamate sensor iGluSnFR. Nat Methods 15, 936–939. 10.1038/s41592-018-0171-3. [PubMed: 30377363]
54. Rosa JM, Bos R, Sack GS, Fortuny C, Agarwal A, Bergles DE, Flannery JG, and Feller MB (2015). Neuron-glia signaling in developing retina mediated by neurotransmitter spillover. Elife 4. 10.7554/eLife.09590.
55. Wilson JR, Friedlander MJ, and Sherman SM (1984). Fine structural morphology of identified X- and Y-cells in the cat's lateral geniculate nucleus. Proc R Soc Lond B Biol Sci 221, 411–436. 10.1098/rspb.1984.0042. [PubMed: 6146984]
56. Marshel JH, Kaye AP, Nauhaus I, and Callaway EM (2012). Anterior-posterior direction opponency in the superficial mouse lateral geniculate nucleus. Neuron 76, 713–720. 10.1016/j.neuron.2012.09.021. [PubMed: 23177957]
57. Jacoby J, and Schwartz GW (2018). Typology and Circuitry of Suppressed-by-Contrast Retinal Ganglion Cells. Front Cell Neurosci 12, 269. 10.3389/fncel.2018.00269. [PubMed: 30210298]
58. Tien NW, Pearson JT, Heller CR, Demas J, and Kerschensteiner D (2015). Genetically Identified Suppressed-by-Contrast Retinal Ganglion Cells Reliably Signal Self-Generated Visual Stimuli. J Neurosci 35, 10815–10820. 10.1523/JNEUROSCI.1521-15.2015. [PubMed: 26224863]

59. Martersteck EM, Hirokawa KE, Evarts M, Bernard A, Duan X, Li Y, Ng L, Oh SW, Ouellette B, Royall JJ, et al. (2017). Diverse Central Projection Patterns of Retinal Ganglion Cells. Cell Rep 18, 2058–2072. 10.1016/j.celrep.2017.01.075. [PubMed: 28228269]
60. Jacobs BL, and Fornal CA (1991). Activity of brain serotonergic neurons in the behaving animal. Pharmacol Rev 43, 563–578. [PubMed: 1775508]
61. Cohen JY, Amoroso MW, and Uchida N (2015). Serotonergic neurons signal reward and punishment on multiple timescales. Elife 4. 10.7554/eLife.06346.
62. Li Y, Zhong W, Wang D, Feng Q, Liu Z, Zhou J, Jia C, Hu F, Zeng J, Guo Q, et al. (2016). Serotonin neurons in the dorsal raphe nucleus encode reward signals. Nat Commun 7, 10503. 10.1038/ncomms10503. [PubMed: 26818705]
63. Ren J, Friedmann D, Xiong J, Liu CD, Ferguson BR, Weerakkody T, DeLoach KE, Ran C, Pun A, Sun Y, et al. (2018). Anatomically Defined and Functionally Distinct Dorsal Raphe Serotonin Sub-systems. Cell 175, 472–487 e420. 10.1016/j.cell.2018.07.043. [PubMed: 30146164]
64. Boschert U, Amara DA, Segu L, and Hen R (1994). The mouse 5hydroxytryptamine1B receptor is localized predominantly on axon terminals. Neuroscience 58, 167–182. 10.1016/0306-4522(94)90164-3. [PubMed: 8159291]
65. Fujiyama F, Hioki H, Tomioka R, Taki K, Tamamaki N, Nomura S, Okamoto K, and Kaneko T (2003). Changes of immunocytochemical localization of vesicular glutamate transporters in the rat visual system after the retinofugal denervation. J Comp Neurol 465, 234–249. 10.1002/cne.10848. [PubMed: 12949784]
66. Mizutani H, Hori T, and Takahashi T (2006). 5-HT1B receptor-mediated presynaptic inhibition at the calyx of Held of immature rats. Eur J Neurosci 24, 1946–1954.10.1111/j.1460-9568.2006.05063.x. [PubMed: 17067296]
67. Pape HC, and McCormick DA (1995). Electrophysiological and pharmacological properties of interneurons in the cat dorsal lateral geniculate nucleus. Neuroscience 68, 1105–1125. 10.1016/0306-4522(95)00205-w. [PubMed: 8544986]
68. Huang KW, Ochandarena NE, Philson AC, Hyun M, Birnbaum JE, Cicconet M, and Sabatini BL (2019). Molecular and anatomical organization of the dorsal raphe nucleus. Elife 8. 10.7554/eLife.46464.
69. Duan X, Qiao M, Bei F, Kim IJ, He Z, and Sanes JR (2015). Subtype-specific regeneration of retinal ganglion cells following axotomy: effects of osteopontin and mTOR signaling. Neuron 85, 1244–1256. 10.1016/j.neuron.2015.02.017. [PubMed: 25754821]
70. Rousso DL, Qiao M, Kagan RD, Yamagata M, Palmiter RD, and Sanes JR (2016). Two Pairs of ON and OFF Retinal Ganglion Cells Are Defined by Intersectional Patterns of Transcription Factor Expression. Cell Rep 15, 1930–1944. 10.1016/j.celrep.2016.04.069. [PubMed: 27210758]
71. Krieger B, Qiao M, Rousso DL, Sanes JR, and Meister M (2017). Four alpha ganglion cell types in mouse retina: Function, structure, and molecular signatures. PLoS One 12, e0180091. 10.1371/journal.pone.0180091.
72. Lovinger DM, Mateo Y, Johnson KA, Engi SA, Antonazzo M, and Cheer JF (2022). Local modulation by presynaptic receptors controls neuronal communication and behaviour. Nat Rev Neurosci. 10.1038/s41583-022-00561-0.
73. Sari Y (2004). Serotonin1B receptors: from protein to physiological function and behavior. Neurosci Biobehav Rev 28, 565–582. 10.1016/j.neubiorev.2004.08.008. [PubMed: 15527863]
74. Bouhelal R, Smounya L, and Bockaert J (1988). 5-HT1B receptors are negatively coupled with adenylate cyclase in rat substantia nigra. Eur J Pharmacol 151, 189–196. 10.1016/0014-2999(88)90799-6. [PubMed: 2971554]
75. Foster KA, Kreitzer AC, and Regehr WG (2002). Interaction of postsynaptic receptor saturation with presynaptic mechanisms produces a reliable synapse. Neuron 36, 1115–1126. 10.1016/s0896-6273(02)01106-6. [PubMed: 12495626]
76. Dodge FA Jr., and Rahamimoff R (1967). On the relationship between calcium concentration and the amplitude of the end-plate potential. J Physiol 189, 90P–92P.
77. Neher E, and Sakaba T (2008). Multiple roles of calcium ions in the regulation of neurotransmitter release. Neuron 59, 861–872. 10.1016/j.neuron.2008.08.019. [PubMed: 18817727]

78. Filosa A, Barker AJ, Dal Maschio M, and Baier H (2016). Feeding State Modulates Behavioral Choice and Processing of Prey Stimuli in the Zebrafish Tectum. Neuron 90, 596–608. 10.1016/j.neuron.2016.03.014. [PubMed: 27146269]
79. Yoshida M, Sasa M, and Takaori S (1984). Serotonin-mediated inhibition from dorsal raphe nucleus of neurons in dorsal lateral geniculate and thalamic reticular nuclei. Brain Res 290, 95–105. 10.1016/0006-8993(84)90739-x. [PubMed: 6692141]
80. McCormick DA, and Bal T (1997). Sleep and arousal: thalamocortical mechanisms. Annu Rev Neurosci 20, 185–215. 10.1146/annurev.neuro.20.1.185. [PubMed: 9056712]
81. Pape HC, and McCormick DA (1989). Noradrenaline and serotonin selectively modulate thalamic burst firing by enhancing a hyperpolarization-activated cation current. Nature 340, 715–718. 10.1038/340715a0. [PubMed: 2475782]
82. Zhang Y, Kim IJ, Sanes JR, and Meister M (2012). The most numerous ganglion cell type of the mouse retina is a selective feature detector. Proc Natl Acad Sci U S A 109, E2391–2398. 10.1073/pnas.1211547109. [PubMed: 22891316]
83. Hoy JL, Yavorska I, Wehr M, and Niell CM (2016). Vision Drives Accurate Approach Behavior during Prey Capture in Laboratory Mice. Curr Biol 26, 3046–3052. 10.1016/j.cub.2016.09.009. [PubMed: 27773567]
84. Yang YC, Hu CC, and Lai YC (2015). Non-additive modulation of synaptic transmission by serotonin, adenosine, and cholinergic modulators in the sensory thalamus. Front Cell Neurosci 9, 60. 10.3389/fncel.2015.00060. [PubMed: 25852468]
85. Lam YW, and Sherman SM (2013). Activation of both Group I and Group II metabotropic glutamatergic receptors suppress retinogeniculate transmission. Neuroscience 242, 78–84. 10.1016/j.neuroscience.2013.03.043. [PubMed: 23558090]
86. Born G, Schneider-Soupiadis FA, Erisken S, Vaiceliunaite A, Lao CL, Mobarhan MH, Spacek MA, Einevoll GT, and Busse L (2021). Corticothalamic feedback sculpts visual spatial integration in mouse thalamus. Nat Neurosci 24, 1711–1720. 10.1038/s41593-021-00943-0. [PubMed: 34764474]
87. Reinhold K, Resulaj A, Scanziani M (2021). Brain state-dependent modulation of thalamic visual processing by cortico-thalamic feedback. BioRxiv 2021.*10.04.463017*.
88. Rowan S, and Cepko CL (2004). Genetic analysis of the homeodomain transcription factor Chx10 in the retina using a novel multifunctional BAC transgenic mouse reporter. Dev Biol 271, 388–402. 10.1016/j.ydbio.2004.03.039. [PubMed: 15223342]
89. Madisen L, Mao T, Koch H, Zhuo JM, Berenyi A, Fujisawa S, Hsu YW, Garcia AJ 3rd, Gu X, Zanella S, et al. (2012). A toolbox of Cre-dependent optogenetic transgenic mice for light-induced activation and silencing. Nat Neurosci 15, 793–802. 10.1038/nn.3078. [PubMed: 22446880]
90. Duan X, Krishnaswamy A, De la Huerta I, and Sanes JR (2014). Type II cadherins guide assembly of a direction-selective retinal circuit. Cell 158, 793–807. 10.1016/j.cell.2014.06.047. [PubMed: 25126785]
91. Scott MM, Wylie CJ, Lerch JK, Murphy R, Lobur K, Herlitze S, Jiang W, Conlon RA, Strowbridge BW, and Deneris ES (2005). A genetic approach to access serotonin neurons for in vivo and in vitro studies. Proc Natl Acad Sci U S A 102, 16472–16477. 10.1073/pnas.0504510102. [PubMed: 16251278]
92. Chen TW, Wardill TJ, Sun Y, Pulver SR, Renninger SL, Baohan A, Schreiter ER, Kerr RA, Orger MB, Jayaraman V, et al. (2013). Ultrasensitive fluorescent proteins for imaging neuronal activity. Nature 499, 295–300. 10.1038/nature12354. [PubMed: 23868258]
93. Klapoetke NC, Murata Y, Kim SS, Pulver SR, Birdsey-Benson A, Cho YK, Morimoto TK, Chuong AS, Carpenter EJ, Tian Z, et al. (2014). Independent optical excitation of distinct neural populations. Nat Methods 11, 338–346. 10.1038/nmeth.2836. [PubMed: 24509633]
94. Lin JY, Knutsen PM, Muller A, Kleinfeld D, and Tsien RY (2013). ReaChR: a red-shifted variant of channelrhodopsin enables deep transcranial optogenetic excitation. Nat Neurosci 16, 1499–1508. 10.1038/nn.3502. [PubMed: 23995068]
95. Welsh CA, Stephany CE, Sapp RW, and Stevens B (2020). Ocular Dominance Plasticity in Binocular Primary Visual Cortex Does Not Require C1q. J Neurosci 40, 769–783. 10.1523/JNEUROSCI.1011-19.2019. [PubMed: 31801811]

96. Zhang SX, Lutas A, Yang S, Diaz A, Fluhr H, Nagel G, Gao S, and Andermann ML (2021). Hypothalamic dopamine neurons motivate mating through persistent cAMP signalling. Nature 597, 245–249. 10.1038/s41586-021-03845-0. [PubMed: 34433964]

97. Lutas A, Fernando K, Zhang SX, Sambangi A, and Andermann ML (2022). History-dependent dopamine release increases cAMP levels in most basal amygdala glutamatergic neurons to control learning. Cell Rep 38, 110297. 10.1016/j.celrep.2022.110297. [PubMed: 35081349]

98. Niell CM, and Stryker MP (2008). Highly selective receptive fields in mouse visual cortex. J Neurosci 28, 7520–7536. 10.1523/JNEUROSCI.0623-08.2008. [PubMed: 18650330]

99. Turner J, and Salt T (1998). Characterization of sensory and corticothalamic excitatory inputs to rat thalamocortical neurones in vitro. The Journal of Physiology 510, 829–843. [PubMed: 9660897]

100. Chen C, and Regehr WG (2000). Developmental remodeling of the retinogeniculate synapse. Neuron 28, 955–966. 10.1016/s0896-6273(00)00166-5. [PubMed: 11163279]

101. Hauser JL, Edson EB, Hooks BM, and Chen C (2013). Metabotropic glutamate receptors and glutamate transporters shape transmission at the developing retinogeniculate synapse. J Neurophysiol 109, 113–123. 10.1152/jn.00897.2012. [PubMed: 23076103]

102. Hauser JL, Liu X, Litvina EY, and Chen C (2014). Prolonged synaptic currents increase relay neuron firing at the developing retinogeniculate synapse. J Neurophysiol 112, 1714–1728. 10.1152/jn.00451.2014. [PubMed: 24966302]

103. Kingston AE, Ornstein PL, Wright RA, Johnson BG, Mayne NG, Burnett JP, Belagaje R, Wu S, and Schoepp DD (1998). LY341495 is a nanomolar potent and selective antagonist of group II metabotropic glutamate receptors. Neuropharmacology 37, 1–12. 10.1016/s0028-3908(97)00191-3. [PubMed: 9680254]

104. Yang YC, Hu CC, Huang CS, and Chou PY (2014). Thalamic synaptic transmission of sensory information modulated by synergistic interaction of adenosine and serotonin. J Neurochem 128, 852–863. 10.1111/jnc.12499. [PubMed: 24147740]

105. Jones JR, Simon T, Lones L, and Herzog ED (2018). SCN VIP Neurons Are Essential for Normal Light-Mediated Resetting of the Circadian System. J Neurosci 38, 7986–7995. 10.1523/JNEUROSCI.1322-18.2018. [PubMed: 30082421]

106. Wang Q, Ding SL, Li Y, Royall J, Feng D, Lesnar P, Graddis N, Naeemi M, Facer B, Ho A, et al. (2020). The Allen Mouse Brain Common Coordinate Framework: A 3D Reference Atlas. Cell 181, 936–953 e920. 10.1016/j.cell.2020.04.007. [PubMed: 32386544]

107. Kerschensteiner D, and Guido W (2017). Organization of the dorsal lateral geniculate nucleus in the mouse. Vis Neurosci 34, E008. 10.1017/S0952523817000062. [PubMed: 28965501]

108. Mitra PP, and Pesaran B (1999). Analysis of dynamic brain imaging data. Biophys J 76, 691–708. 10.1016/S0006-3495(99)77236-X. [PubMed: 9929474]

109. Pachitariu M, Stringer C, Schrö S, Dipoppa M, Rossi LF, Carandini M, and Harris KD (2016). Suite2p: beyond 10,000 neurons with standard two-photon microscopy. bioRxiv 10.1101/061507.

110. Kerlin AM, Andermann ML, Berezovskii VK, and Reid RC (2010). Broadly tuned response properties of diverse inhibitory neuron subtypes in mouse visual cortex. Neuron 67, 858–871. 10.1016/j.neuron.2010.08.002. [PubMed: 20826316]

Highlights

- Serotonin suppresses retinal axon spike-evoked presynaptic Ca^{2+} and glutamate release
- Suppression was stronger in retinal axons driven by full-field luminance change
- Serotonin and arousal suppress different subsets of retinal axons in thalamus
- Serotonergic suppression may scale with 5-HT1B expression in retinal axonal boutons

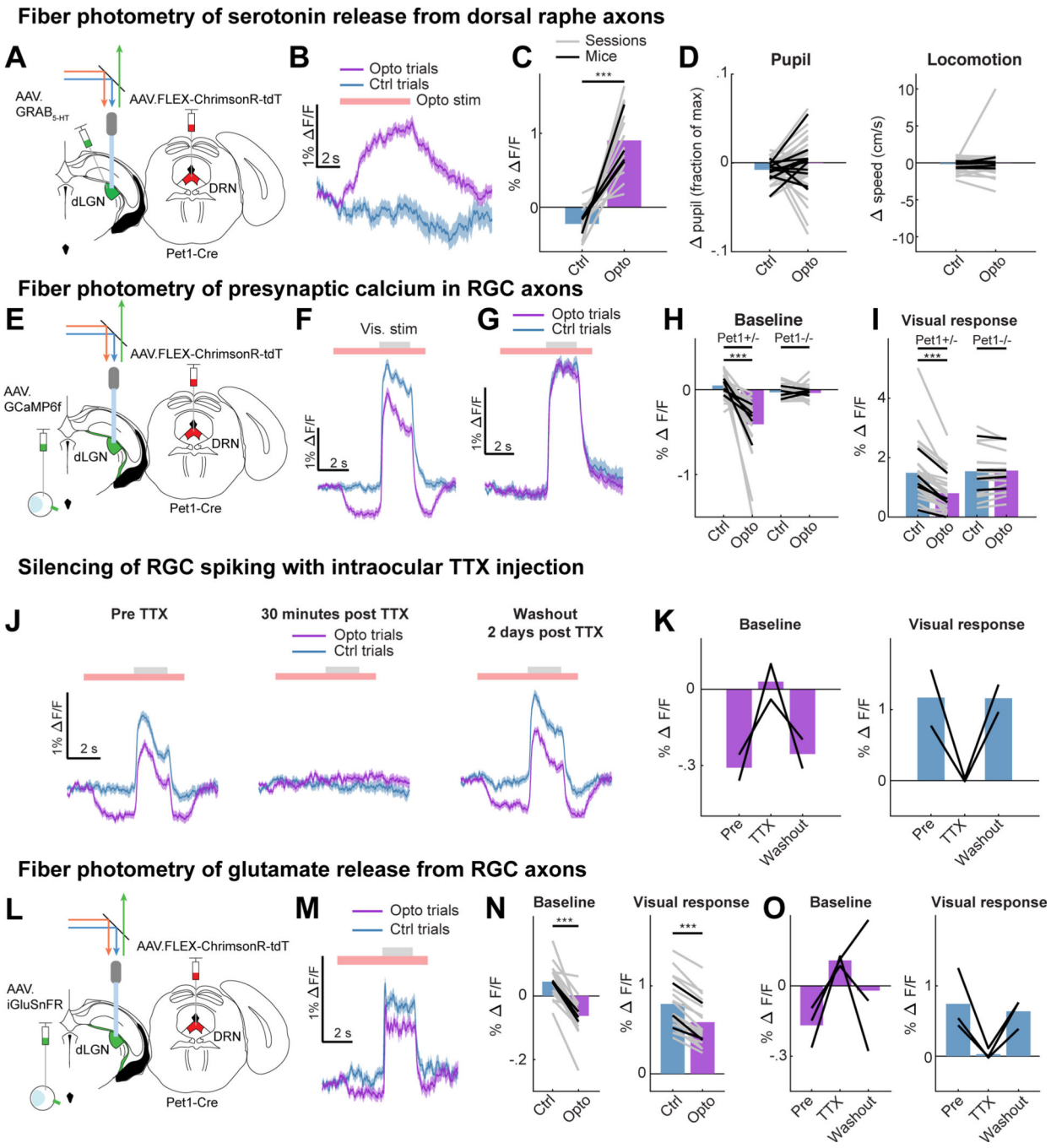

Figure 1. DRN$^{5HT→dLGN}$ stimulation releases serotonin and suppresses spiking-evoked calcium signals and glutamate release from RGC axons

A. Set-up in awake head-fixed mice for fiber photometry recordings of GRAB$_{5\text{-}HT}$ expressed in dLGN, with optogenetic stimulation (optostim) of DRN$^{5HT→dLGN}$ axons (ChrimsonR-tdT injected in DRN of Pet1-Cre mice).

B. Example GRAB$_{5\text{-}HT}$ trace of fractional change in fluorescence (ΔF/F) on trials with ('Opto') and without ('Ctrl') optostim (red bar).

C. Mean GRAB$_{5\text{-}HT}$ ΔF/F on Opto and Ctrl trials (18 sessions [gray lines], 4 mice [black lines]). ***p<0.001, linear mixed effects model (LME).

D. Mean change in pupil area (*left*, normalized to maximum pupil size in the recording session) and running speed (*right*) on Opto and Ctrl trials (41 and 45 sessions, 11 and 12 mice for pupil size and running, respectively, LME: p = 0.21 for pupil, p = 0.50 for running).
E. Set-up for fiber photometry of calcium signals (GCaMP6f) from RGC axons, with optostim of $DRN^{5HT \rightarrow dLGN}$ axons.
F. Example calcium activity trace on Ctrl and Opto trials. Gray bar: visual drifting grating.
G. Same as F but for Pet1-$Cre^{-/-}$ mice that lacked ChrimsonR expression.
H. Mean baseline calcium ΔF/F (mean luminance gray screen) on Opto and Ctrl trials in Pet1-$Cre^{+/-}$ mice (27 sessions [gray lines], 5 mice [black lines]) and Pet1-$Cre^{-/-}$ mice (16 sessions, 4 mice). LME: Pet1-$Cre^{+/-}$, ***p<0.001; Pet1-$Cre^{-/-}$, p = 0.84.
I. Same as H but for visual responses ($\Delta F/F_0$, F_0 = mean of 2 s before optogenetic stimulation). LME: Pet1-$Cre^{+/-}$,***p<0.001; Pet1-$Cre^{-/-}$, p = 0.67.
J. Example calcium activity traces from the same mouse before, 30 minutes after and 2 days after TTX injection into the contralateral eye.
K. Mean baseline calcium ΔF/F on Opto trials (*left*) and visual response on Ctrl trials (*right*) before, 30 min after and 2 days after TTX. Black lines: mice (n = 2).
L. Set-up for fiber photometry of iGluSnFR in RGC axons with optostim of $DRN^{5HT \rightarrow dLGN}$ axons.
M. Example trace of glutamate release on Ctrl and Opto trials (red bar). Gray bar: time of visual stimulation.
N. Mean baseline (*left*) and visually-evoked (*right,* $\Delta F/F_0$, F_0 = mean of 2 s before optogenetic stimulation) glutamate release on Ctrl and Opto trials (18 sessions [gray lines], 3 mice [black lines]). LME: ***p<0.001.
O. Same as K but for iGluSnFR recordings. Black lines: mice (n = 3).
Error bars in B,F,G,J,M: mean +/− SEM across trials. See also Figure S1.

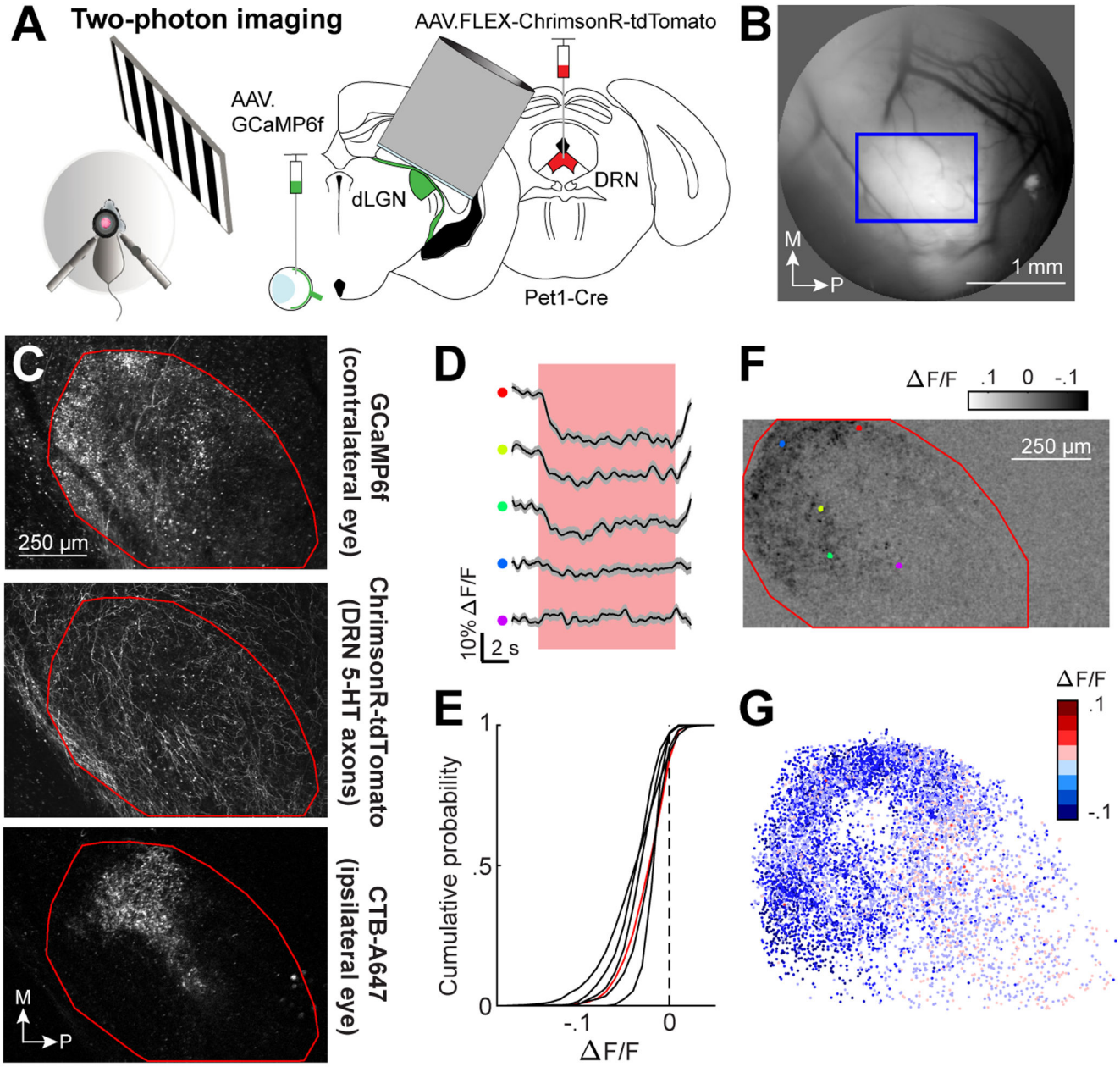

Figure 2. DRN$^{5HT→dLGN}$ stimulation suppresses baseline calcium in individual RGC boutons

A. Set-up in awake head-fixed mice for two-photon imaging of GCaMP6f in RGC boutons from the contralateral eye, with optostim of DRN$^{5HT→dLGN}$ axons (ChrimsonR-tdT in DRN of Pet1-Cre mice).

B. Epifluorescence imaging of the surface of thalamus through the cannula. The bright region indicates GCaMP6f-expressing RGC axons within the dLGN. Blue box: two-photon imaging field of view (FOV).

C. Example two-photon FOV of the entire dorsolateral surface of dLGN. *Top*: GCaMP6f in RGC axons. *Middle*: ChrimsonR-tdT in DRN axons. *Bottom:* ipsilateral retinal projection ('ipsi patch') labelled with CTB-A647. Red line: dLGN outline.

D. ΔF/F time course of five individual RGC boutons from the example FOV in C during optostim of $DRN^{5HT \rightarrow dLGN}$ axons for 10 s (red bar) at baseline. Color indicates location in dLGN (see F). Mean +/− SEM across trials.

E. Cumulative distribution across boutons of amplitude of optostim-evoked suppression of calcium activity at baseline. 6,299 boutons, 6 mice [black lines]. Red line: FOV in C and F. All distributions were significantly suppressed, LME: $p < .001$.

F. Optostim-evoked change in ΔF/F at baseline for FOV in C.

G. RGC boutons from 6 mice after morphological alignment, colored by amplitude of optostim-evoked suppression at baseline.

See also Figure S2.

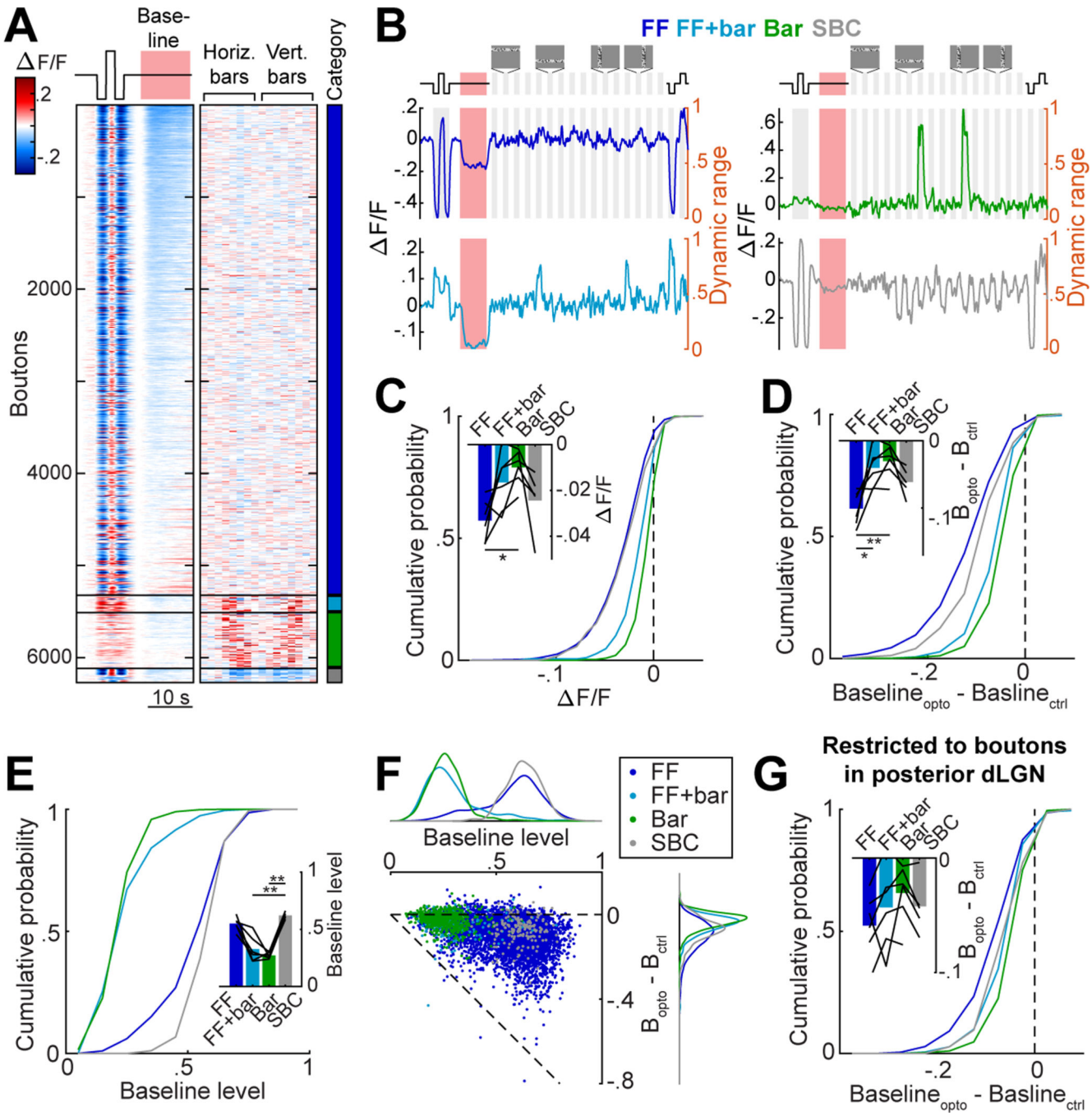

Figure 3. DRN$^{5HT→dLGN}$ optogenetic stimulation preferentially suppresses RGC boutons with high baseline activity and sensitivity to luminance changes

A. Heatmap of mean concatenated responses of boutons to stepwise luminance changes, to DRN$^{5HT→dLGN}$ optostim at baseline (*left*), and to horizontal and vertical bars containing white noise (*middle*, see Fig. S3A, Movie S1 and Methods). Boutons are separated by category (color bar, *right*) and sorted by amplitude of suppression during DRN$^{5HT→dLGN}$ stimulation (red bar) at baseline. FF: 5,333, Bar: 599, FF+bar: 189, SBC: 178 boutons.

B. Mean concatenated responses of an example bouton from each category to stepwise luminance changes, DRN$^{5HT→dLGN}$ stimulation (red area), and vertical and horizontal

white-noise bars. Activity levels were normalized to the bouton's dynamic range (right y-axis): the range between the minimum and maximum activity (re-scaled to 0–1) across all stimulus types (see Methods).

C. Cumulative distributions of response to optostim at baseline for each category. LME: all distributions were significantly suppressed, $p < .001$; FF vs. Bar, FF vs. FF+Bar, SBC vs. FF+Bar, SBC vs. Bar $p<.001$, FF+Bar vs. Bar $p < .01$. Inset: mean per mouse (black lines, n = 6) and across mice (bars). Mouse means for FF vs. Bar: *p <.05 (Kruskal-Wallis, with post hoc Dunn's multiple comparison).

D. Cumulative distributions of difference in baseline (normalized to dynamic range) on Opto and Ctrl trials. LME: all distributions were significantly suppressed, $p < .001$; FF vs. Bar, FF vs. FF+Bar, SBC vs. FF+Bar, SBC vs. Bar, FF vs. SBC: $p<.001$. Inset: mean per mouse (black lines, n = 6) and across mice (bars). Mouse means for FF vs. Bar: **p <.01, FF vs. FF+Bar: *p<.05 (Kruskal-Wallis with post hoc Dunn's).

E. Cumulative distributions of mean activity during baseline (normalized to dynamic range). Inset: mean per mouse (black lines, n = 6) and across mice (bars). Mouse means for FF+bar vs. SBC, and SBC vs. Bar: **p <.01 (Kruskal-Wallis with post hoc Dunn's).

F. Scatter plot of baseline activity vs. suppression by optostim (as in D). Dots: RGC boutons, colored by category. *Top and right*: distributions for each category. Pearson's correlation across all boutons: −.379, $p = 9 \times 10^{-215}$.

G. Same as D, but restricted to the posterior region of dLGN containing retinotopic responses to bar stimuli. LME: all categories were significantly suppressed, $p < .001$; FF vs. Bar, FF vs. FF+Bar, $p<.001$, SBC vs. Bar, $p<.01$. Inset: mean per mouse (black lines, n = 6) and across mice (bars).

See also Figure S3 and Movie S1.

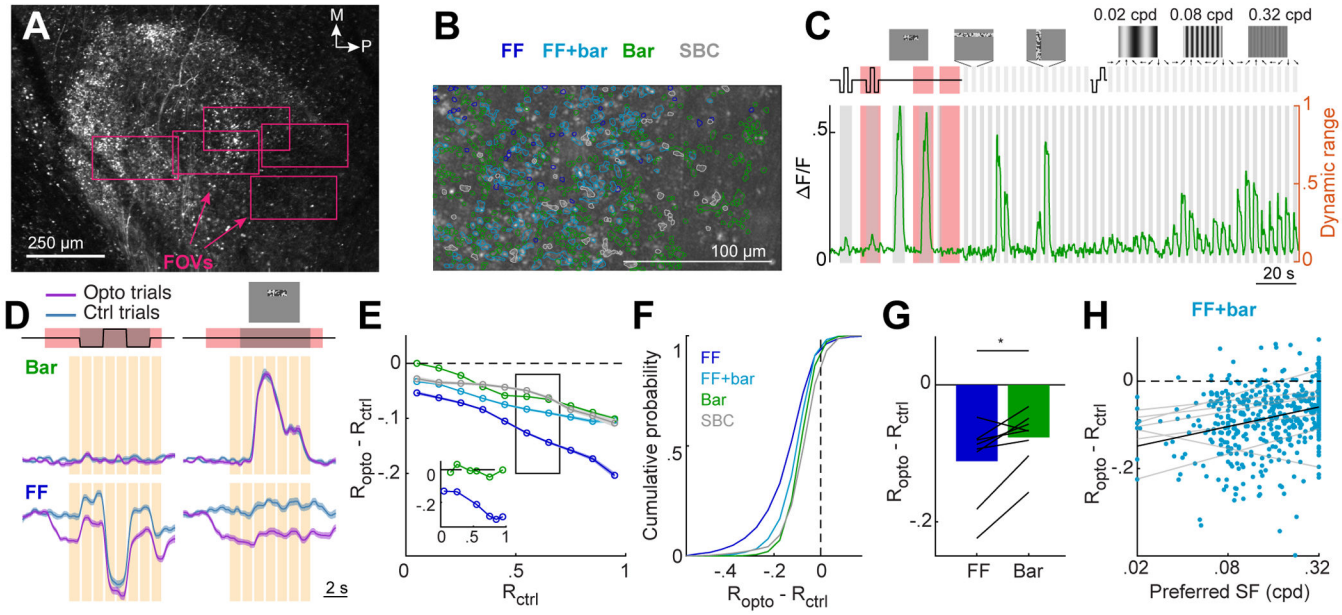

Figure 4. Selective suppression during DRN$^{5HT→dLGN}$ stimulation is not due to floor effects

A. Low magnification two-photon image of RGC axons in dLGN. Rectangles: FOVs imaged at higher magnification on different sessions.

B. Example FOV. ROIs: individual RGC boutons, colored by category.

C. Example trace of the mean concatenated response of a Bar bouton. Gray shaded regions: visual stimulus presentation. Red shaded regions: DRN$^{5HT→dLGN}$ optostim. Activity levels were normalized to the bouton's dynamic range (right y-axis).

D. Mean concatenated response of a FF and a Bar bouton to a 6-s luminance step and a 6-s sequence of small bars containing binarized white noise (*top,* see also Movie S2) on Ctrl and Opto trials. Mean +/− SEM across trials. Orange bars: time points at which the difference between the Ctrl (R_{ctrl}) and Opto (R_{opto}) trials is calculated.

E. Mean suppression due to optostim (R_{opto} - R_{ctrl}) across boutons in each category as a function of dynamic range level, Rctrl. Lines: mean +/− SEM across boutons. FF: 2,049, FF+bar: 1,416, Bar: 3,736, SBC: 713 boutons (20 FOV, 9 mice). Inset: optostim-evoked suppression for the FF (blue) and Bar bouton (green) in D.

F. Cumulative distribution of optostim-evoked suppression, for time points when each bouton's activity was within 0.5–0.7 of its dynamic range on Ctrl trials (black rectangle in E). LME: all distributions were significantly suppressed, $p < .001$; FF vs. Bar, FF vs. FF+Bar, SBC vs. Bar, SBC vs. FF+Bar, SBC vs. FF $p<.001$. FF: 1947, FF+bar: 1306, Bar: 3343, SBC: 708 boutons (20 FOV, 9 mice).

G. Mean suppression by optostim (as in F) for FF and Bar boutons. Bar: means across mice; black lines: mean per mouse (n=8). *$p<0.05$, two-tailed paired t-test.

H. Scatter plot for FF+bar boutons of optostim-evoked suppression vs. spatial frequency preference (824 boutons). Only boutons driven by drifting gratings were included. Pearson's correlation across all boutons: .287, $p = 2.3 \times 10^{-11}$. Gray and black lines: linear fits per mouse and across mice.

See also Fig. S4G. See also Figure S4.

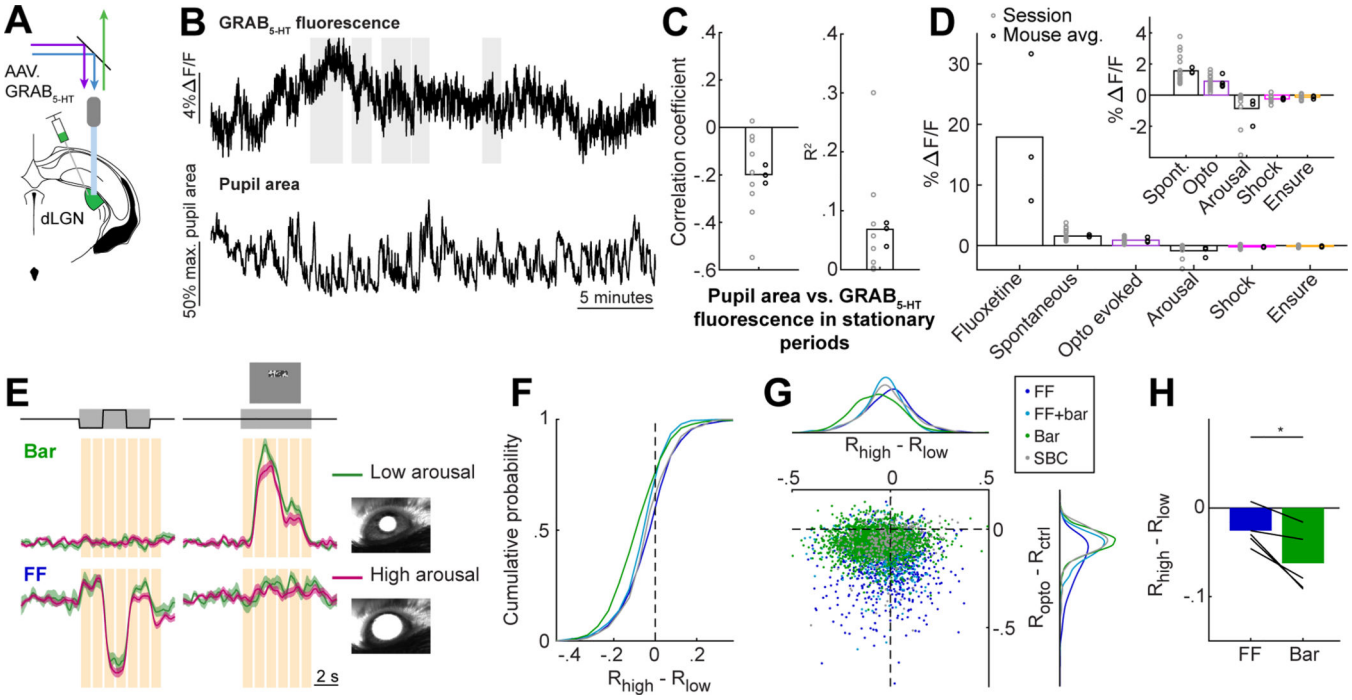

Figure 5. Different RGC boutons are suppressed by arousal and by serotonin

A. Set-up for dual color (465 nm/405 nm) fiber photometry recordings of $GRAB_{5\text{-}HT}$ expressed in dLGN. Recordings at 405 nm were used to correct for motion artifact (Fig. S5A).

B. Example traces of $GRAB_{5\text{-}HT}$ ΔF/F and pupil area. Gray bars: stationary periods.

C. Correlation between pupil area and $GRAB_{5\text{-}HT}$ ΔF/F in stationary periods (Pearson's correlation coefficient and R^2 of linear regression).

D. Changes in $GRAB_{5\text{-}HT}$ fluorescence related to fluoxetine (Fig. S1D), optostim (Fig. 1B-C), standard deviation of spontaneous fluctuations (panel B and Fig. S1E), arousal ($\Delta F/F_{high} - \Delta F/F_{low}$), tail shock (Fig. S5C), and Ensure (Fig. S5B). n = 4 mice (optostim) or 3 mice (all others). Inset: expanded y axis scale.

E. Mean responses of same example boutons as in Fig. 4D, averaged separately for control trials with high arousal (magenta; pupil >50% of maximum) and low arousal (green; pupil <50% of maximum). Mean +/− SEM across trials. Orange bars: time points at which the difference between the high arousal (R_{high}) and low arousal (R_{low}) trials is calculated.

F. Cumulative distributions of $R_{high} - R_{low}$, for time points when each bouton's activity was between .5-.7 of its dynamic range. LME: all distributions except SBC were significantly suppressed, $p < .001$; FF vs. Bar, FF vs. FF+Bar, SBC vs. Bar, SBC vs. FF+Bar, $p<.001$, SBC vs. FF $p<.05$. FF: 885, FF+bar: 805, Bar: 2051, SBC: 313 boutons (8 FOV, 5 mice).

G. Scatterplot of suppression by optostim vs. by arousal. Suppression by arousal and optostim showed only a weak negative correlation ($r = -0.047$, $p < 0.001$; consistent with Fig. 5C). Dots: RGC boutons, colored by category. *Top and right*: distributions per category.

H. Mean suppression by arousal in FF and Bar boutons (compare to Fig. 4G). Bars: means across mice; lines: means per mouse (n=5). *p<0.05, two-tailed paired t-test.

See also Figure S5.

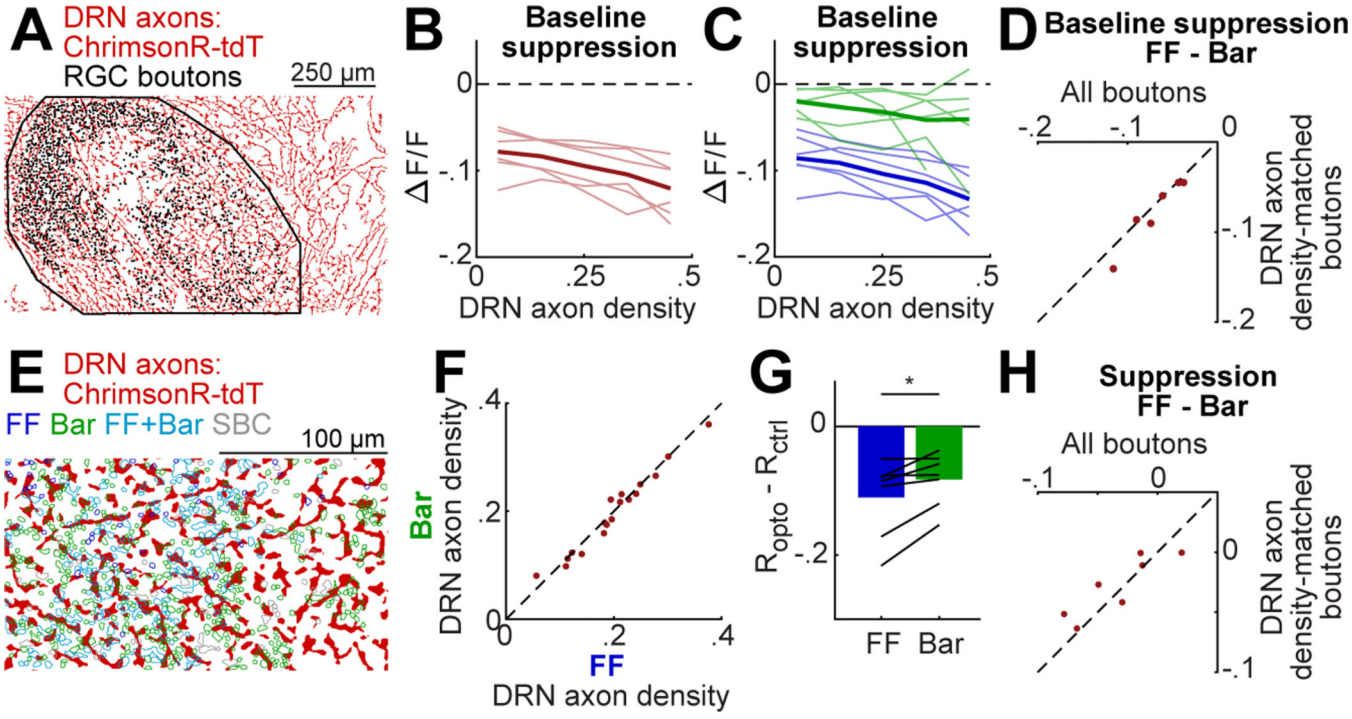

Figure 6. Local DRN axon density does not explain stronger serotonergic suppression of FF boutons

A. Binarized image of DRN axons in dLGN (see Fig. 2C). Dots: bouton locations. Black line: dLGN outline.

B. Mean suppression by $DRN^{5HT \rightarrow dLGN}$ optostim at baseline as a function of nearby DRN axon density (fraction of pixels with a DRN axon in a 10 µm radius of a bouton's center of mass, see Methods). Thin lines: mean per mouse (n = 6), thick line: mean across mice.

C. Same as B, but plotted separately for FF and Bar boutons.

D. Mean difference in optostim-evoked suppression between FF and Bar boutons, calculated using all boutons or using only boutons with nearby DRN axon density between .25-.4 (i.e. 'axon density-matched boutons').

E. Binarized image of DRN axons (red) in a high-magnification FOV (Fig. 4). RGC bouton ROIs are colored by category.

F. Mean DRN axon density around FF vs. Bar boutons for each FOV.

G. Mean optostim-evoked suppression (see Fig. 4G) for FF and Bar boutons at .5-.7 of their dynamic range, restricted to boutons with DRN axon density between .15 and .3. Bars: mean across mice; black lines: means per mouse (n=8). *p<0.05, two-tailed paired t-test.

H. Mean difference per mouse in optostim-evoked suppression between FF and Bar boutons using all boutons (as in Figure 4G) or subsets of boutons with nearby DRN axon density between .15 and .3.

See also Figure S6.

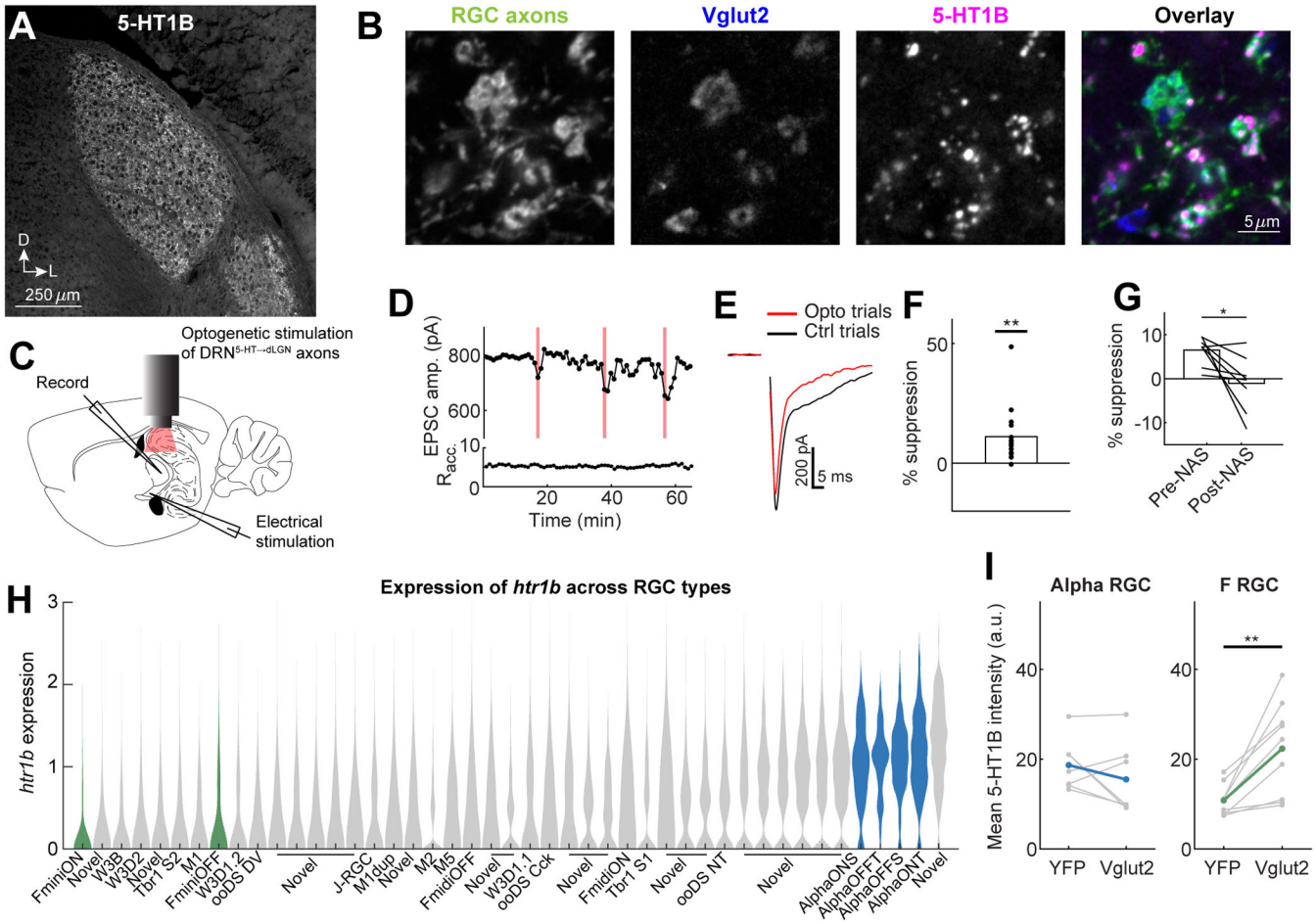

Figure 7. 5-HT1B is localized to RGC boutons and mediates DRN$^{5HT→dLGN}$ -evoked suppression

A. Coronal slice of dLGN immunostained for 5-HT1B.

B. Example colocalization of 5-HT1B puncta (magenta) with Vglut2 (blue, RGC axon terminals) and RGC axons (green, Chx10-Cre; FLEX-ChR2-YFP).

C. Set-up of whole-cell recording of thalamocortical cells in a dLGN slice from Pet1-Cre mice. EPSCs are evoked by optic tract electrical stimulation with and without optostim of ChrimsonR-expressing DRN axons.

D. Plot of the peak EPSC amplitude (holding potential: −70 mV) and access resistance ($R_{acc.}$) over consecutive trials of optic tract stimulation. Red bars: optostim trials.

E. Example EPSC from the recording in D on Opto and Ctrl trials (Ctrl, mean of five preceding trials). Stimulus artifacts are blanked for clarity.

F. Mean percent suppression across all 16 recorded cells (dots) from 14 mice. **p<0.01, two-tailed t-test.

G. Mean percent suppression before and after bath application of NAS-181. DRN$^{5HT→dLGN}$-evoked suppression was reduced by NAS-181 in 7/8 cells (black lines). *p<0.05, two-tailed paired t-test.

H. Violin plot of *htr1b* expression (in log Transcripts Per Million [TPM]) in all molecularly-defined RGC types (publicly available scSeq dataset of adult RGCs). Green: F-mini RGCs, blue: alpha RGCs.

I. Mean intensity of 5-HT1B staining within all Vglut2+ regions of interest (ROIs) in a slice, compared with ROIs that overlapped with specific RGC axons (labeled with YFP using Kcng4-Cre mice [alpha RGCs] or Foxp2-Cre mice [F-mini RGCs], see Methods). Kcng4-Cre: 7 slices [gray lines], 3 mice, Foxp2-Cre: 9 slices, 4 mice; colored lines: mean across slices. **p<0.01, two-tailed paired t-test (F-mini RGC: p = 0.0042; alpha RGC: p = 0.253).

See also Figure S7.

KEY RESOURCES TABLE

REAGENT or RESOURCE	SOURCE	IDENTIFIER
Antibodies		
Rabbit polyclonal anti-5HT1b	Abcam	Ab13896
Guinea pig polyclonal anti-vglut2	Millipore	AB2251
Chicken polyclonal anti-GFP	Invitrogen	A10262
Bacterial and virus strains		
AAV2/2.CAG.GcaMP6f.WPRE.SV40	Boston children's viral core	
AAV2/1.hSyn.FLEX.ChrimsonR-tdTomato	Klapoetke et al. (2014)	UNC Vector Core
AAV2/2.hSyn.FLEX.ReaChR.mCitrine	Boston children's viral core	
AAV2/9.hSyn.$GRAB_{5\text{-}HT2h}$	WZ Biosciences	
AAV2/1.hSyn.GCaMP6f.WPRE.SV40	Chen et al. (2013)	Addgene, #100837
AAV2/1.hSyn.iGluSnFR.A184S	Marvin et al. (2018)	Addgene, #106174
Chemicals, peptides, and recombinant proteins		
CTB-Alexa647	Thermo Fisher Scientific	C34778
NAS-181	Tocris biosciences	#1413
CGP-55845	Tocris	Cat #1248
Deposited data		
Retinal Ganglion Cell recordings	Goetz et al. 2022	RGCtypes.org
Adult RGC single cell sequencing	Tran et al. (2019)	https://singlecell.broadinstitute.org/single_cell/study/SCP509
Allen Mouse Brain Connectivity Atlas	Martersteck et al. (2017)	http://connectivity.brain-map.org/
Experimental models: Organisms/strains		
Mouse: ePet-Cre	Jackson	RRID: IMSR_JAX: 012712
Mouse: Foxp2-Cre	Jackson	RRID: IMSR_JAX:030541
Mouse: Kcng4-Cre	Jackson	RRID: IMSR_JAX:029414
Mouse: Chx10-Cre	Cepko Lab	RRID: IMSR_JAX: 005105
Mouse: Ai32	Jackson	RRID: IMSR_JAX: 012569
Software and algorithms		
MATLAB R2017a	MathWorks	https://www.mathworks.com/products/matlab.html
Igor Pro 6.12	Wavemetrics	https://www.wavemetrics.com/products/igorpro/igorpro.htm;RRID:SCR_000325
Suite2p	Pachitariu et al. (2016)	https://github.com/cortex-lab/Suite2P
PsychToolBox	PsychToolBox	http://psychtoolbox.org/
Scanbox	Neurolabware	https://scanbox.org/
NIMH MonkeyLogic	NIMH	https://monkeylogic.nimh.nih.gov/
Other		
Two-photon microscope	Neurolabware	http://neurolabware.com/
InSightX3 laser	Spectra-Physics	InSightX3
10x .6 NA objective	Olympus	